

Characterization of the Spatial Resolution for the Scintillator Crystal CLYC for GN-VISION



EMJMD in Nuclear Physics

Gaston Emanuel Cisterna

Tutor

Jorge Lerendegui-Marco

July, 2024

Abstract

Contents

1	Introduction	1
1.1	Motivation	1
1.1.1	Particle Therapy (PT) Advancements and Monitoring Challenges .	1
1.1.2	National Security and Nuclear Energy Industry	2
1.1.3	GN-VISION	3
1.2	Radiation Detection	4
1.2.1	Scintillation crystals	4
1.2.2	Monolithic Crystals	5
1.2.3	Pixelated Crystals	6
1.3	Photosensors: PMTs and SiPMs	6
1.4	The i-TED Concept	8
1.4.1	State-of-the-Art and Motivation	8
1.4.2	i-TED Design	8
1.4.3	Compton Imaging	8
2	GN-Vision: Imaging for Gamma Rays and Neutrons	11
2.1	Overview of GN-Vision	11
2.2	Core Components and Configuration	11
2.3	Electronics and Readout Systems: Transition from I-TED to GN-Vision .	14
2.3.1	I-TED Electronics and Readout System	14
2.3.2	Challenges with Individual Read-Outs and Charge Modulation Solutions	15
2.4	GN-Vision Readout	16
2.4.1	Encoder Weights and Event Position Calculation	17
2.5	Objective	18

3 Materials and methods	20
3.1 Gamma Radiation	20
3.2 Neutron Radiation	23
4 Results Gamma Irradiation	25
4.1 Gamma-Ray Event Selection	25
4.2 Interaction Position Reconstruction	26
4.3 GEANT4 Simulations	30
5 Results Neutron Irradiation	37
5.1 Figure of Merit for PSD Evaluation	38
6 Performance of GN-VISION	42
6.1 Gamma-ray Simulation	43
6.2 Neutron Simulation	46
7 Conclusions	49
Bibliography and References	49
Appendix	51
A	51
B	52

CHAPTER 1

Introduction

1.1 Motivation

This chapter provides an overview of GN-Vision, outlining the foundational motivations and the specific needs that this advanced imaging technology aims to address. Building on the principles established in the i-TED project, GN-Vision enhances the capabilities for imaging thermalized neutrons and gamma rays, focusing particularly on challenges in medical applications, national security, and nuclear energy sectors.

1.1.1 Particle Therapy (PT) Advancements and Monitoring Challenges

Particle therapy, particularly utilizing proton and carbon ion beams, is increasingly recognized for its efficacy in treating solid cancers. Light ion beams possess unique dose distribution profiles, making them highly effective in targeting tumors while sparing healthy tissues compared to traditional X-ray treatments.

Another alternative, Boron Neutron Capture Therapy (BNCT), suitable for bad-prognosis cases with a ramified morphology, involves injecting tumors with Boron-10 [13, 14]. With an interaction cross-section a thousand times greater than elements found in human tissue, when thermalized neutrons interact with Boron-10 they produce highly ionizing particles: ^7Li and ^4He , as well as 478 keV prompt γ ray causing tumor cell death.

However, the spatial selectivity presents challenges in accurately monitoring dose delivery. Numerous factors contribute to uncertainty in dose release positioning during particle therapy and BNCT treatments: computed tomography (CT) image calibration, morphological changes between imaging and treatment sessions, patient positioning errors, organ motion

during treatment and complexities raised from factors such as imaging software and analytical Monte-Carlo-Method-based Simulations [6–10]. Moreover, concerns regarding dose deposition far from the treated area and secondary cancer risks from emitted neutrons have emerged [11, 12]. Real-time monitoring during treatment could enhance quality assurance and treatment efficacy. Figure 4.2.3 provides an example of this context. The images show a phantom irradiated with neutrons of 95 MeV and 100 MeV, respectively. After irradiation, imaging was performed through p- γ reaction, resulting in the images shown. Profiles were then obtained at the center of the beam in each image, demonstrating how each curve correlates with the Bragg peak for the two energies. This correlation illustrates the impact of dose distribution and highlights the importance of accurate dose delivery and real-time monitoring.

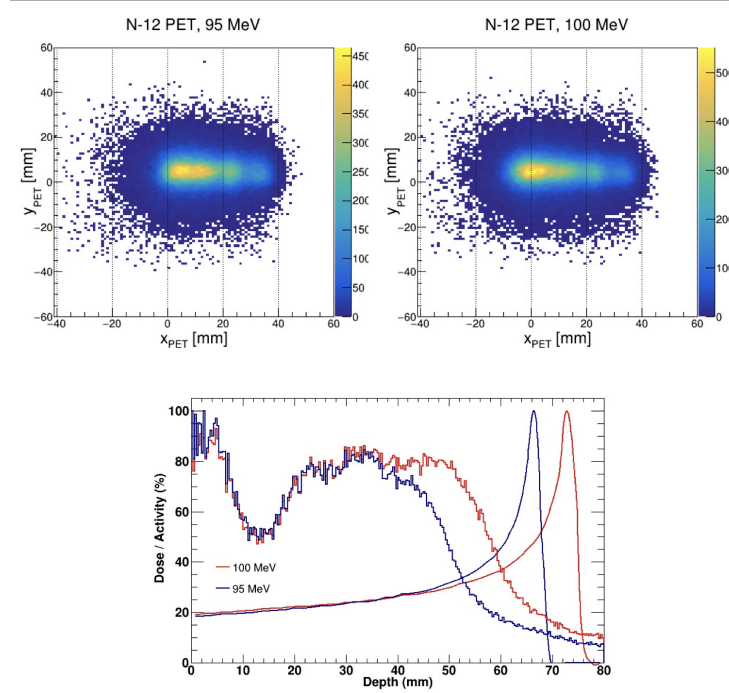


Figure 1.1.1: Example of phantom irradiation with 95 MeV and 100 MeV proton, followed by imaging with p- γ reactions. The profiles at the beam center correlate with the Bragg peak for the respective energies.

1.1.2 National Security and Nuclear Energy Industry

The International Atomic Energy Agency (IAEA) emphasizes that illicit trafficking and theft of nuclear materials can result in nuclear proliferation and the creation of improvised

nuclear or radiological dispersal devices. In 2022 alone, a total of 168 incidents of illegal or unauthorized activities involving nuclear and other radioactive material were reported by 31 States (an increase of 22 incidents from 2022), according to the IAEA's annual fact sheet summarizing data from the IAEA Incident and Trafficking Database (ITDB)]. Detecting and responding to these acts are essential for effective nuclear security.



Figure 1.1.2: The number of the incidents recorded in ITDB during the period 1993–2023 is 4243. \square

1.1.3 GN-VISION

To tackle these challenges, this work studies a device capable of imaging thermalized neutrons and gamma rays simultaneously. Such a device would enable real-time dosimetry in BNCT, monitor secondary doses in both particle therapy (PT) and BNCT, and work with Prompt Gamma-Ray Imaging (PGI) for in-vivo range verification in particle therapy. Such a device would not only advance treatment monitoring but also enhance radiation source localization and risk assessment in nuclear inspections.

Likewise, in the context of nuclear safety, this system might effectively identifying materials that may pose risks. Such a system allows for the precise detection of hazardous materials, enabling their seizure or appropriate handling to prevent injury or other damage to public safety and security. Unlike conventional checkpoint detectors, this system also has the capability to perform imaging to pinpoint the source of emission accurately. Additionally, the system can be portable, which provides a significant advantage. This feature is particularly useful in monitoring radioactive waste and is essential for managing spent fuel in both research and electricity-generating nuclear reactors.

1.2 Radiation Detection

A brief introduction to the principles of neutron and gamma ray imaging, including the physics underlying the technologies used, such as Compton imaging and scintillation detectors will be explained. This theoretical foundation will help clarify how GN-Vision operates at a technical level and how it represents an improvement over existing systems.

First, It's provided a brief examination of scintillating detectors coupled to Silicon Photomultipliers (SiPM) and Photomultipliers Tube (PMT), specifically chosen for their application in detecting ionizing radiation within the imaging system under consideration. We will delve into their technical specifications, operational principles, and significance in the field of radiation detection and imaging technology.

1.2.1 Scintillation crystals

The use of inorganic scintillation crystals as radiation detectors are based on their electronic properties, more specifically, their electronic structure band. An electron placed in the valence band can be excited due to ionizing radiation, and it can then be placed in either the conduction band or the exciton band, creating a hole in the valence band that can be filled with a de-excited electron with the subsequent scintillation light emission. Higher the energy of the incident radiation, higher the amount of electrons placed in the conduction band, and thus higher the scintillation of visible photons. These visible photons are collected then by a photosensors to quantify the energy of the incident radiation.

Good examples of Scintillation crystals are $\text{LaBr}_3(\text{Ce})$ and $\text{LaCl}_3(\text{Ce})$. Key attributes that influence the performance of scintillation detectors include:

- **Emission Spectra:** It is crucial for the crystal to be transparent to the light it emits, requiring a clear separation between its absorption and emission spectra in order for light to escape from the crystal.
- **Scintillation Yield:** This refers to the number of photons generated per unit of energy deposited, which determines the sensitivity of the detector.
- **Fast Time Response:** The capability to emit light rapidly is vital for the accurate and timely recording of radiation events.
- **Refractive Index:** The refractive index of the crystal should be matched to that of the waveguide to minimize light loss.

These crystals can be categorized into two main types: monolithic and pixelated, each with distinct characteristics and applications.

1.2.2 Monolithic Crystals

Monolithic crystals are single, continuous pieces of scintillating material. They are valued for their simplicity and efficiency in collecting light. A monolithic crystal typically offers:

- **Uniform Scintillation Response:** As there are no boundaries within the crystal, the scintillation light is evenly produced and collected, ensuring a consistent response across the entire detector.
- **Ease of Production:** Manufacturing a single piece of crystal is generally simpler and less costly than producing multiple small pixels.
- **Large Volume Detection:** These crystals are capable of detecting radiation over large volumes, making them ideal for applications where a wide area needs to be covered.



Figure 1.2.1: Caption

1.2.3 Pixelated Crystals

Pixelated crystals consist of an array of small, discrete crystal elements, each acting as an independent scintillator. This structure is particularly advantageous for:

- **Fixed Spatial Resolution:** Each pixel can be read independently, thus the size of the pixels represent the resolution that might be achieved.
- **Modularity:** Pixel arrays can be easily configured into various shapes and sizes to fit specific detector geometries.
- **Reduced Crosstalk:** By isolating the scintillation events to individual pixels, these crystals minimize optical crosstalk, enhancing the quality of the signal.

Both types of crystals play crucial roles in radiation detection systems, with the choice between monolithic and pixelated crystals largely depending on the specific needs of the application, such as the required resolution, detection efficiency, and geometric flexibility.

1.3 Photosensors: PMTs and SiPMs

Accompanying these scintillators in the detection process are photosensors, which transform the emitted light into electrical signals proportional to the energy of the incident radiation. The most common types of photosensors used are Photomultiplier Tubes (PMTs) and Silicon Photomultipliers (SiPMs).

In PMTs, the visible light emitted by the crystal generates photo-electrons in the photocathode. These electrons are accelerated and multiplied through a series of electrodes

(dynodes) at high potentials (around 1500 V), resulting in a detectable output current. PMTs are extremely sensitive detectors of light (UV, visible, and near-IR) with amplification up to 10^8 (160 dB). They have low noise and fast response. However, PMTs require high voltage (300 to 2000 V) sources to operate, are sensitive to magnetic fields, and are very expensive and delicate.

SiPMs, on the other hand, are single-photon-sensitive devices based on single-photon avalanche diodes (SPADs). In SiPMs, each photodiode operates in Geiger mode, creating an avalanche when it detects a photon. SiPMs work with low light levels to ensure one photon per photodiode, allowing the total number of photons to be counted by summing the avalanches from each photodiode, providing a final signal as the contribution of individual photodiodes.

Compared to conventional PMTs, SiPMs have a more deterministic photoelectron gain, resulting in a higher signal-to-noise ratio (SNR) for a fixed number of detected photons. They are cheaper due to mass production, require much lower bias voltages, and offer higher quantum efficiency in the red to near-infrared range. However, SiPMs have higher dark current at a given temperature, potentially requiring subambient cooling, which increases complexity and cost. Large active areas are difficult to achieve due to higher dark counts.



Figure 1.3.1: Caption 1

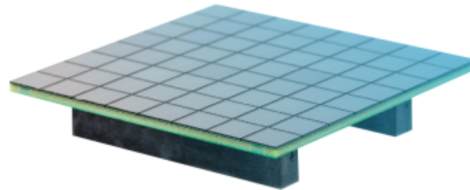


Figure 1.3.2: Caption 2

1.4 The i-TED Concept

1.4.1 State-of-the-Art and Motivation

GN-Vision was building upon the foundational technologies developed for I-TED. I-TED system was designed to significantly improve the signal-to-background ratio in neutron capture measurements by utilizing the Compton imaging technique. I-TED contributes significantly to the understanding of neutron capture rates by doing photon imaging with the gammas produced in neutron reactions. This topic is crucial for advancing nuclear physics research related to stellar evolution and nucleosynthesis.

1.4.2 i-TED Design

The i-TED module utilizes two detector planes as shown in Figure 1.4.1. The first plane comprises a Scatter Position Sensitive Detector or Scatter PSD, a single $50 \times 50 \times 15$ mm LaCl_3 scintillation crystal, that allows to capture the initial energy and positions of photons interacting through a Compton scattering. The second plane is a PSD Absorber. The absorber plane consists of 4 thicker $50 \times 50 \times 25$ mm LaCl_3 scintillation crystals centered with the scatter, recording the remaining energy and position. In both cases, each PSD is equipped with pixelated SiPMs of $50 \times 50 \text{ mm}^2$, which are sensitive enough to detect the position and energy of the scattered and absorbed photons accurately. Distance between Scatter and Absorber plane can be varied and controlled between 10 and 60 mm from the back of the scatterer to the front of the absorber.

Usually, there are four modules of Scatter-Absorber pairs, each called a Compton module. This configuration allows for PET imaging, providing 25 planes for coincidence gammas.

1.4.3 Compton Imaging

i-TED employs the Compton imaging technique to reconstruct the path of incoming gamma rays based on the data collected from the scatter and absorber PSDs. An incoming γ -ray interacts with the first detection plane, undergoing Compton scattering, and then deposits the rest of its energy in the second detection plane, where it undergoes photo-absorption. That's why these planes are called scatter and absorber, and their



Figure 1.4.1: Caption

thicknesses are selected to maximize the scattering probability in the former and the full energy absorption in the latter. The energy, position, and time of the γ -ray interactions are registered in each detection stage.

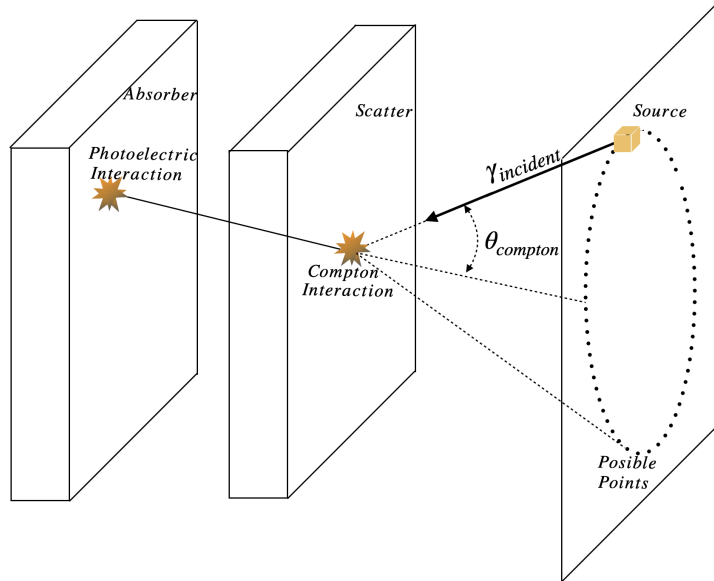


Figure 1.4.2: Caption

The line defined by the two interaction points, r_1 and r_2 , becomes the axis of a virtual

cone whose opening angle $\theta_{compton}$ is given by the Compton formula in 1.1, where m_e is the mass of the electron at rest, c the speed of light, E_2 the energy deposited in the second interaction, and E_γ the energy of the γ -ray. The latter is assumed to be equal to the sum of energies deposited in both detection planes $E_\gamma = E_1 + E_2$.

$$\theta_{compton} = \arccos \left(1 - m_e c^2 \left(\frac{1}{E_2} - \frac{1}{E_\gamma} \right) \right) \quad (1.1)$$

The wall of the cone contains all possible directions of the incoming radiation. The intersection of the cone with a vertical plane located at which the sample position is (hereafter image plane) forms an ellipse. The ellipse passes through the point where the sample is located. The intersection of the Compton cone with the image plane can be leads to the following quadratic equation:

$$[u_x(x_s - a_x) + u_y(y_s - a_y) + u_z(z_s - a_z)]^2 = \cos^2 \theta [(x_s - a_x)^2 + (y_s - a_y)^2 + (z_s - a_z)^2],$$

where u_i with $i = x, y, z$ are the components of a unit vector along the cone axis, a_i are the coordinates of the first interaction in the scatter detector, and (x_s, y_s, z_s) represents the position of the sample. The convergence of multiple cones signifies the location of the radiation source.

It should be note that i-TED registers the interaction positions and energies in each coincidence so that each event in one plane can be corresponded with the same "photon" in the other plane and thus allowing to trace a virtual cone.

GN-Vision: Imaging for Gamma Rays and Neutrons

2.1 Overview of GN-Vision

GN-Vision is an advanced imaging system designed for the dual detection and analysis of gamma rays and neutrons. It builds upon the technological foundation established by the i-TED system, incorporating significant enhancements to address specific challenges in high-resolution, real-time radiation imaging. Fig. 2.1.1 depicts the main components of GN-Vision. Essentially, it includes the PSD scatter and absorber from i-TED, but with an additional pinhole collimator made of polyethylene that has been enriched with lithium-6, called PE⁶Li, to effectively collimate neutrons. Additionally, the scatter crystal has been replaced from LaCl₃ to CLYC6. Each of these components contributes to the overall performance and accuracy of the GN-Vision system and will be explained next.

2.2 Core Components and Configuration

One of the possibilities studies during this project is the employment of Cs₂LiYCl₆ (CLYC) monolithic crystals as Scatter PSD for GN-Vision, in contrast with LaCl₃ for I-TED. CLYC is a type of scintillator crystal known for its ability to detect both gamma rays and thermal neutrons. This dual functionality is due to its unique chemical composition:

- **Cs₂**: Cesium enhances the gamma-ray detection efficiency.
- **Li**: Enriched with ⁶Li, it has a high neutron capture cross-section.
- **YCl₆**: Yttrium chloride forms the crystal structure and affects its scintillation prop-

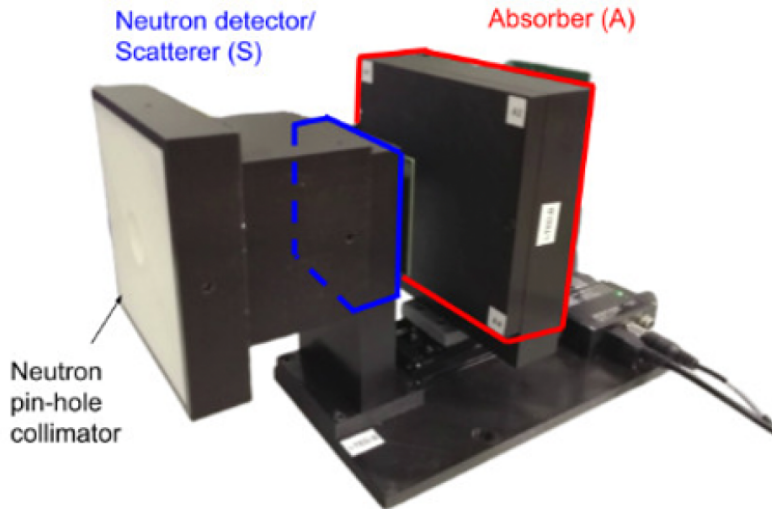
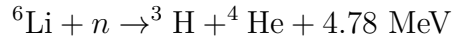


Figure 2.1.1: Main components of the GN-Vision system.

erties.

Neutron detection in CLYC crystals is primarily facilitated by the ${}^6\text{Li}$ component through the following nuclear reaction:



This reaction is exothermic, releasing kinetic energy that is subsequently converted into scintillation light as the reaction products (tritium and alpha particles) interact with the crystal lattice.

Each CLYC crystal is coupled with an array of silicon photomultipliers (SiPMs) for efficient photon detection.

For gamma imaging, GN-VISION inherits the same technique used for i-TED, Compton Imaging. As for neutron imaging, GN-Vision employs a pinhole collimator to focus incoming radiation onto the detector array. The collimator material under study is PE ${}^6\text{Li}$, which contains ${}^6\text{Li}$ with 95% purity. However, the use of natural ${}^6\text{Li}$ is also being studied for cost reduction reasons. The aperture size is carefully controlled to ensure high-resolution imaging while maintaining sufficient throughput of radiation. This design is particularly effective for applications requiring precise localization of radiation sources. The dimensions and performance characteristics of the pinhole collimator were thoroughly studied in ?? and will be addressed in chapter??.

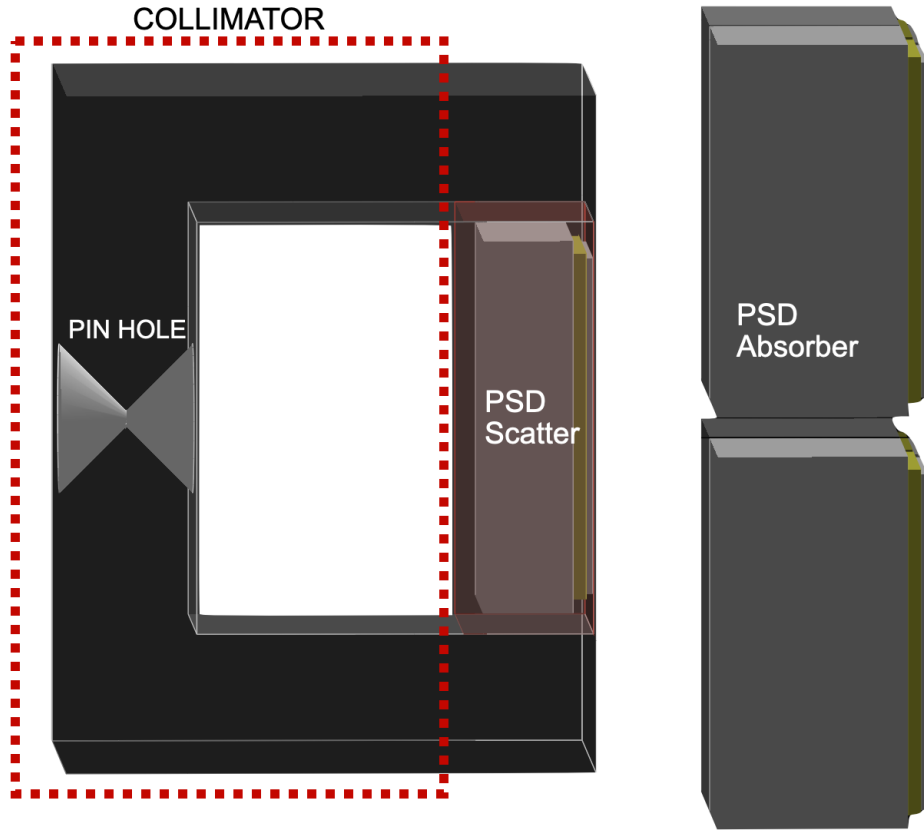


Figure 2.2.1: Caption

In order to distinguish Neutrons from Gamma, Pulse Shape Discrimination (PSD) is a critical feature in GN-Vision. To achieve so, the specific reactions of each particle type must be considered, focusing on the characteristics of the product charged particles in each event sequence. For gamma ray and neutron events, these particles are electrons and alpha particles (and tritium), respectively. A crucial distinction between these product particles lies in their mass, with electrons being relatively lighter. This difference is vividly captured in the generated pulse shapes, allowing for effective discrimination between gamma ray and neutron interactions.

The system captures these differences by integrating the scintillation pulses within two specifically defined time windows, W1 and W2, to distinguish between the quick spikes associated with gamma rays and the prolonged tails characteristic of neutron interactions. This method is essential for accurately categorizing the type of radiation detected, enhancing the system's reliability in complex detection scenarios.

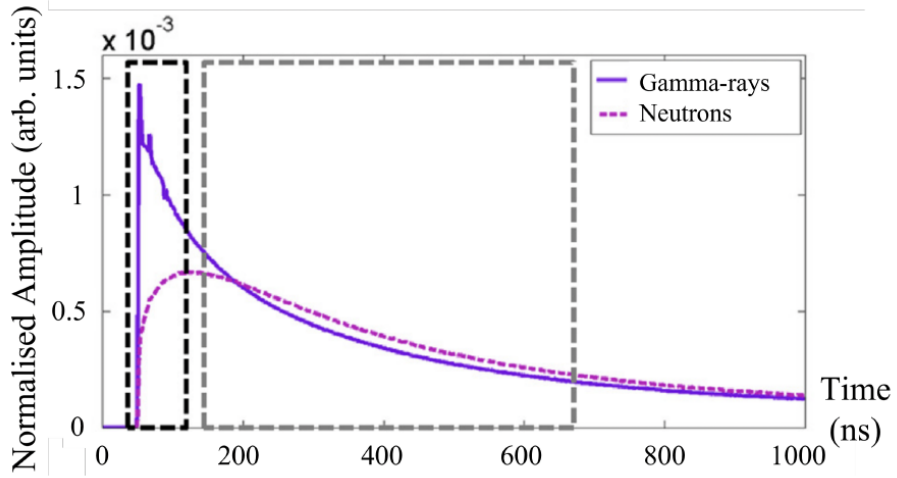


Figure 2.2.2: Caption

2.3 Electronics and Readout Systems: Transition from I-TED to GN-Vision

2.3.1 I-TED Electronics and Readout System

The i-TED system presents a substantial number of 1280 output signal in the complete system with the four modules. Managing such a high number of signals traditionally would necessitate an impractical amount of cabling and componentry.

To manage this complexity, I-TED utilizes an integrated SiPM readout system developed by PETsys Electronics. This system consolidates numerous functions into compact integrated circuit modules, significantly reducing the spatial and logistical demands of the readout process. The system consists of two primary components: the front-end and the back-end modules. The front-end houses PETsys ToFPET2 application-specific integrated circuits (ASICs), essentially 64-channel digitizers capable of reading out an entire SiPM, while the back-end is equipped with FPGA boards that process the data collected by the ASICs. This modular setup was initially crafted for medical imaging but has been adeptly repurposed for Compton imaging applications within I-TED, highlighting its versatility and performance efficacy.

2.3.2 Challenges with Individual Read-Outs and Charge Modulation Solutions

In transitioning from i-TED to GN-Vision for Compton imaging, one might initially consider simply replacing the PSD of the LaCl_3 scatterer with CLYC, while keeping the SiPMs connected to the ASICs and the existing readout electronic. However, significant issues arise due to the inherent disparities between CLYC and LaCl_3 . CLYC exhibits a significantly lower light yield of 20,000 photons per MeV compared to the 50,000 photons per MeV characteristic of LaCl_3 . Additionally, the signal width of CLYC, approximately 4-5 μs , is much greater and more diffuse than that of LaCl_3 , which is around 300 ns. Consequently, the light yield per nanosecond in CLYC is approximately 40 times smaller, leading to substantial signal-to-noise ratio challenges when using CLYC with pixelated SiPMs.

Another consideration might be to read out each signal from individual pixels. This would involve directly connecting each output to the DAQ system. However, this approach requires a substantial number of DAQ channels, resulting in scalability issues and increased design complexity.

One way to address these issues is through Charge Modulation-Based Multiplexing (CMBM), which allows for effective signal amplification without sacrificing positional accuracy. Charge Modulation-Based Multiplexing allows to modulate the input charge collected from the SiPM arrays based on charge division (or charge sharing) multiplexing networks. The charge division multiplexing network steers the input charge toward output channels, and the amount of input charge is divided by the impedance between the input channel and each of the multiplexed output channels. This allows the interacted crystal position and photon energy information from the detectors to be encoded. Typically, the charge division multiplexing network is implemented based on resistive chains, followed by signal shaping and amplification stages at the front-end electronics module.

This multiplexing technique is crucial for managing the extended signal widths and reduced light yield per nanosecond associated with CLYC, compared to LaCl_3 . It helps maintain a high signal-to-noise ratio by optimizing the read-out process, thus allowing GN-Vision

to effectively utilize CLYC for advanced imaging applications.

2.4 GN-Vision Readout

One possibility under study is the use of the 4-Channel Readout instrumentation from AiT (model: AB4T-ARRAY64P), incorporating a patented diode-coupled charge division readout technology that is superior to traditional resistive readout methods. This system supports the Onsemi 8x8 array of 6mm SiPMs (ArrayC-60035-64P-PCB and ArrayJ-60035-64P-PCB) with a 4-channel readout mechanism. This means the 64 signals from the SiPM array are encrypted into four encoded position signals (X_+ , X_- , Y_+ , Y_-) for event centroid calculations. This charge division multiplexing condenses the data into these four output channels as seen in ??.

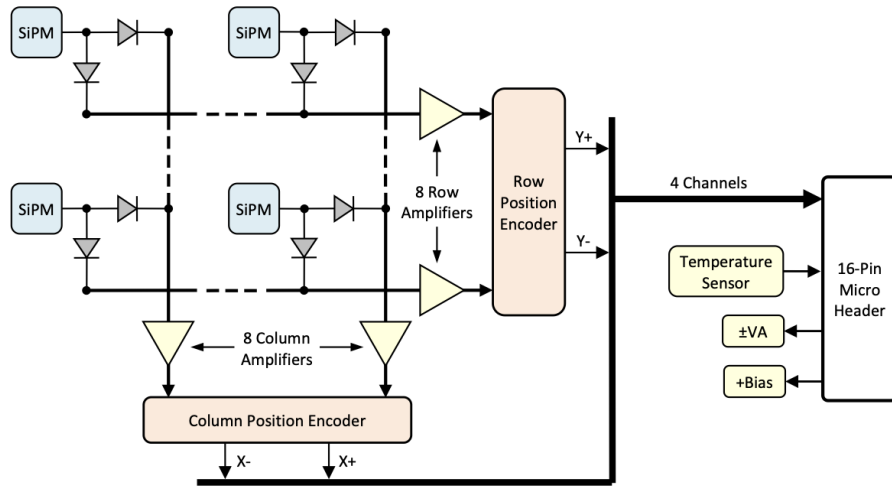


Figure 2.4.1: Caption

The whole AiT readout electronic is depicted in the Figure ???. A power supply feeds the SiPM array (not depicted) through the 4-Channel Active Base Receiver and AB4T-ARRAY64P boards, from 0 to 30V. The SiPM array (coupled to the monolithic CLYC crystal) is connected in the AB4T-ARRAY64P board to then obtain the 4-channel readout for position of interaction reconstruction and an additional channel called Sum. This channel has information of the total charge collected, allowing this system to realize spectroscopy as well. This last channel possesses its own gain and might be varied apart from the 4 channels.

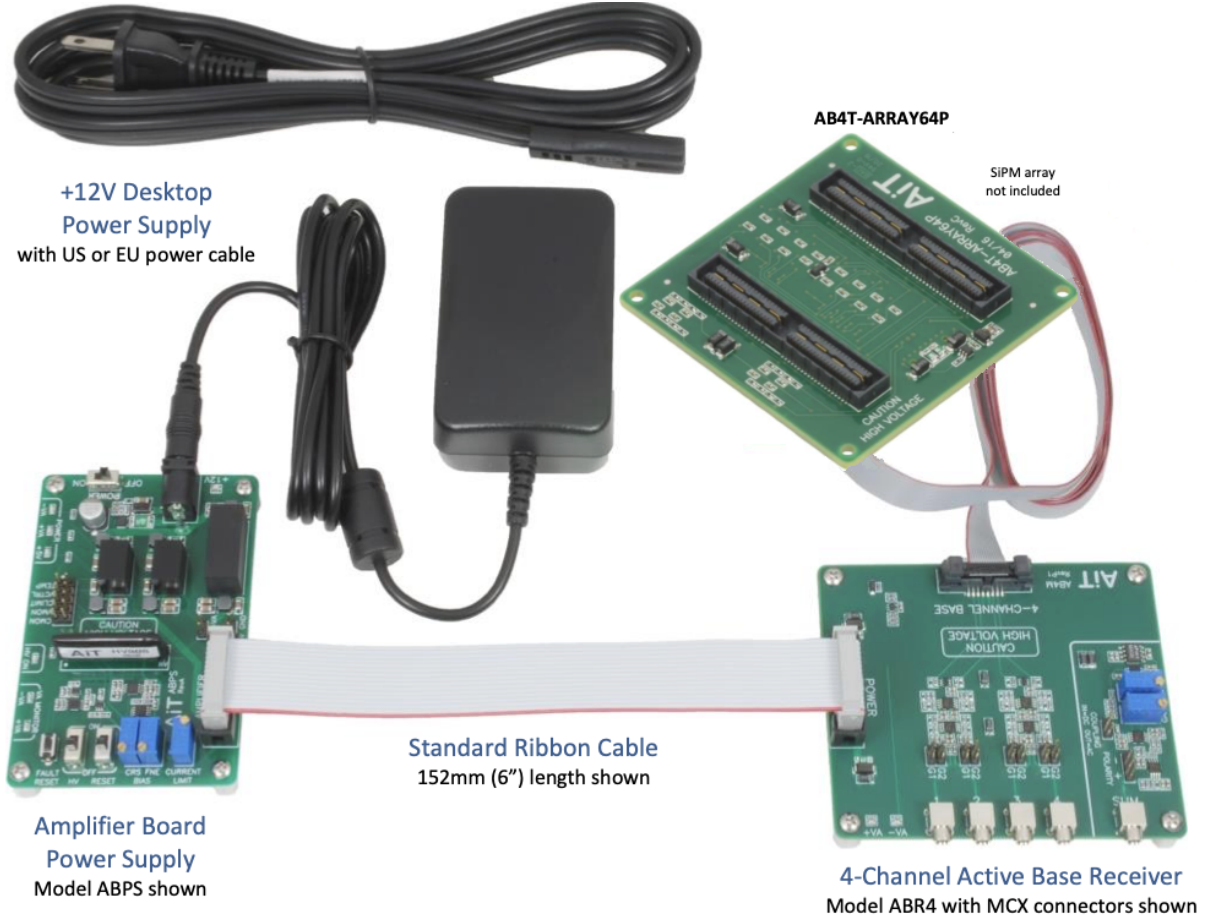


Figure 2.4.2: Caption

2.4.1 Encoder Weights and Event Position Calculation

The rows and columns of the SiPM present encoder weights to obtain the four encoded position signals (X_+ , X_- , Y_+ , Y_-):

$$X_- = (\text{SiPM signal}) \times (\text{encoder gain}) \times (\text{X- fraction})$$

$$X_+ = (\text{SiPM signal}) \times (\text{encoder gain}) \times (\text{X+ fraction})$$

$$Y_- = (\text{SiPM signal}) \times (\text{encoder gain}) \times (\text{Y- fraction})$$

$$Y_+ = (\text{SiPM signal}) \times (\text{encoder gain}) \times (\text{Y+ fraction})$$

The event position is then calculated using:

$$X_{\text{column}} = \frac{(X_+ - X_-)}{(X_+ + X_-)}$$

$$Y_{\text{row}} = \frac{(Y_+ - Y_-)}{(Y_+ + Y_-)}$$

It's interesting to consider how this system behaves when using a monolithic crystal compared to a pixelated crystal. Starting with the latter case, as seen in the picture ??, in a pixelated crystal, individual pixels are activated, and therefore, just one pixel of the SiPM retrieves this signal. In this case, X_{column} and Y_{row} will give the reference position of that activated pixel. The spatial resolution is then fixed by the size of the SiPM pixel.

However, when using a monolithic crystal, light production occurs in a continuous volume, and the diffusion of the light might activate several pixels in the SiPM. This makes X_{column} and Y_{row} dependent on all the activated pixels and on how much light each pixel has received. Consequently, the position of interaction will now be an average weighted by the light collected from all the activated pixels. In this case, the spatial resolution might be different from the size of the SiPM pixel.

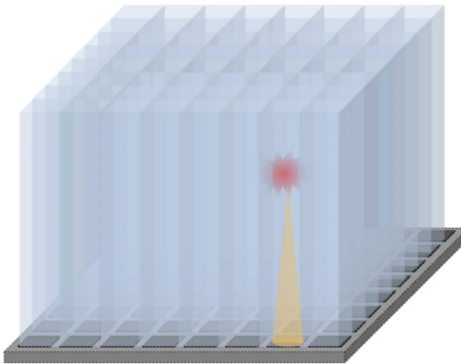


Figure 2.4.3: Caption 1

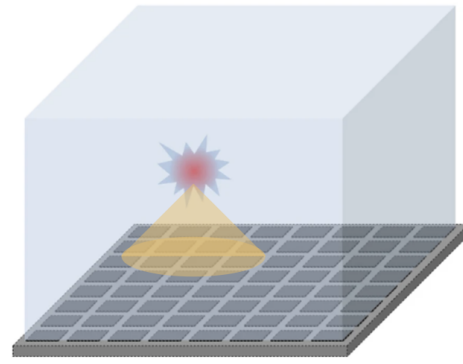


Figure 2.4.4: Caption 2

2.5 Objective

In ??, it has been shown the feasibility of position measurements using monolithic CLYC crystals in conjunction with AiT's Charge Modulation-Based Multiplexing system. Now, the objective is centered on the characterization of the spatial resolution achievable with the CLYC crystal when paired with the AiT readout system for gamma sources.

Our objectives include:

1. **Spatial Resolution Characterization:** Evaluate and quantify the spatial resolution of the CLYC crystal using AiT's Charge Modulation-Based Multiplexing readout system. This will help determine how effectively the system can localize the interaction points of gamma radiation within the crystal.
2. **Linearity Study:** Assess the linearity of the CLYC crystal by studying the reconstruction accuracy of interaction centroids at various positions. This will involve analyzing how accurately the system can reconstruct the interaction points across different spatial locations within the crystal.
3. **Performance Impact on GN-Vision:** Examine the impact of these experimental results on the overall performance of the GN-Vision system. This includes evaluating how the characterized spatial resolution and linearity influence the system's ability to accurately reconstruct the position of the gamma radiation source.

Through these objectives, we aim to enhance the understanding of the GN-Vision system's capabilities and limitations, ultimately improving its performance for high-resolution, real-time gamma and neutron imaging applications.

Materials and methods

3.1 Gamma Radiation

A picture of the whole experimental configuration is shown in Fig. 3.1.1. There are two CLYC scintillator crystals in the configuration, one at the top and one at the bottom. The bottom CLYC crystal is coupled to an 8×8 pixel, $50.44 \times 50.44 \text{ mm}^2$ silicon photomultiplier array (SiPM) from SensL (ArrayJ-60035-65P-PCB). The top CLYC crystal is coupled to a PMT. Each scintillation crystal is coupled with silicon grease. Both crystals, along with the SiPM and PMT respectively, are encapsulated in light-tight black polylactic acid (PLA) plastic housing. The SiPMs are read out using the 4-Channel Readout instrumentation from AiT. Four channels describe the position interaction and a SUM channel describes the total energy deposited in the CLYC. Information from each channel is sent to a CAEN DT5725S DAQ motherboard for further processing.

The systematic spatial characterization in the x - y transverse crystal plane is carried out using a collimated beam of γ -quanta in combination with an x , y -positioning table. The same experimental setup is better detailed in Fig. 3.1.2. The position-sensitive detector under characterization is mounted on a movable platform at the bottom of the experimental setup, while the collimating system, the ^{22}Na source, and the subsidiary detector are fixed on top of a Plexiglas table. The x , y -gantry, which drives the movable platform with the detector under study, corresponds to the T-G-LSM200A200 with a microstep precision of $0.047625 \mu\text{m}$. The ^{22}Na source is sandwiched in a collimating structure under the subsidiary detector to achieve a pencil beam perpendicular to both crystal surfaces. The upper part of the collimator is made of a tungsten parallelepiped with a central hole of 1 mm and 30 mm thickness. Beneath the radioactive sample, a circular tungsten collimator with a central hole of 1 mm and 24 mm effective thickness is placed. An additional

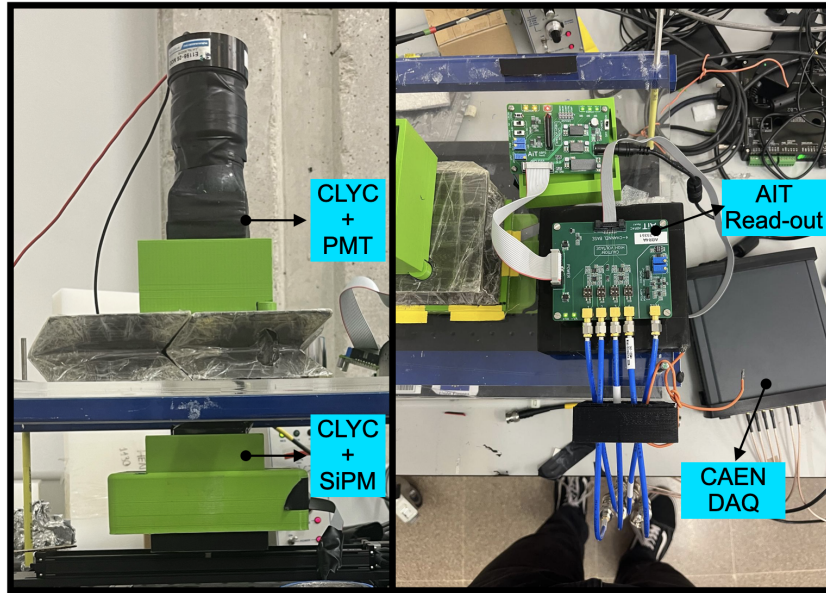


Figure 3.1.1: Caption

lead collimator with a 5.5 cm thickness is positioned beneath the collimating structure. The aperture of this lead collimator is 3 mm in diameter as seen in Fig.3.1.3. In total, accounting for all collimator thicknesses and the distance from the bottom detector to the Plexiglas table, the distance between the front faces of both CLYC crystals in the experimental setup is 26 cm.

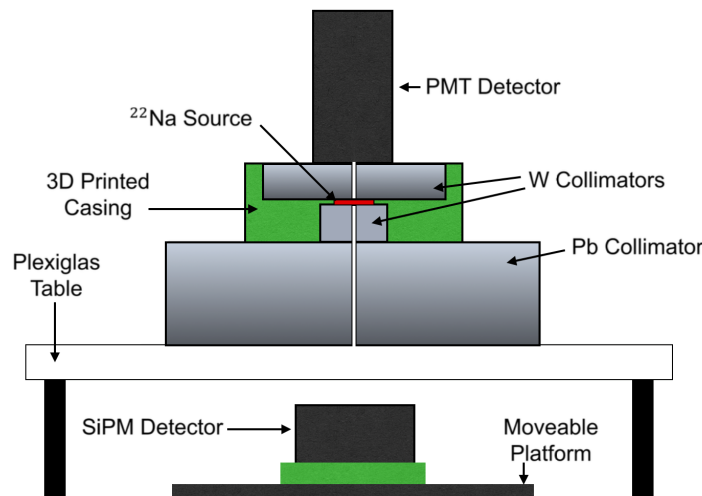


Figure 3.1.2: Caption

Two CLYC crystals operate in time-coincidence mode with a 100 ns coincidence window. Every time one of the five channels exceeds a certain discriminator threshold, the sig-

nal is recorded independently, including channel number, timestamp, shortEnergy, and longEnergy (for pulse discrimination). The signals are recorded in the order they are generated, and it is expected that the four position signals and the sum signal will be grouped together, albeit in random order for each event reaching the crystal. However, some channels present more noise, leading to a higher count rate, typically associated with the sum signal. Thus, the five signals do not always appear grouped together.

An additional channel comes from the PMT signal. The PMT is primarily used for coincidence measurements. Since the goal is to characterize the spatial resolution of the CLYC crystal plus AiT read-out, the best way to filter desired events is by measuring in coincidence. For the analysis, we use only full-energy deposition of the 511 keV annihilation γ -rays emitted from a point-like ^{22}Na source (2 MBq activity). The collimator has a relatively small aperture, resulting in a low count rate and a high signal-to-noise ratio. By measuring in coincidence, the annihilation γ -rays will be recorded with the same timestamp (within a time interval) in different detectors, allowing us to select these events for characterization, effectively eliminating background noise. Additionally, the annihilation γ -rays are more likely to reach the detector through the collimator's aperture, providing a pin-beam for spatial characterization.

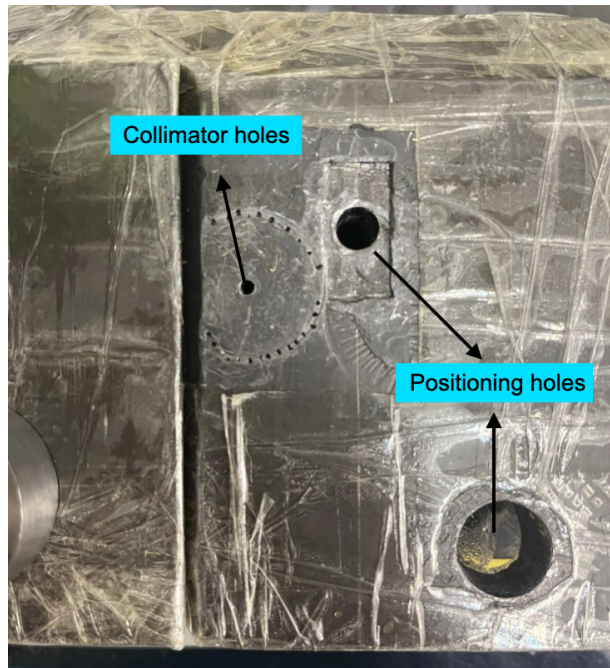


Figure 3.1.3: Caption

3.2 Neutron Radiation

For neutron radiation, the main objectives are to verify the system's capability to distinguish between gamma and neutron radiation and to recreate an interaction position pattern in the detector according to the fixed experimental configuration. The experimental setup, as shown in Figure 3.2.1, was carried out in the lab.

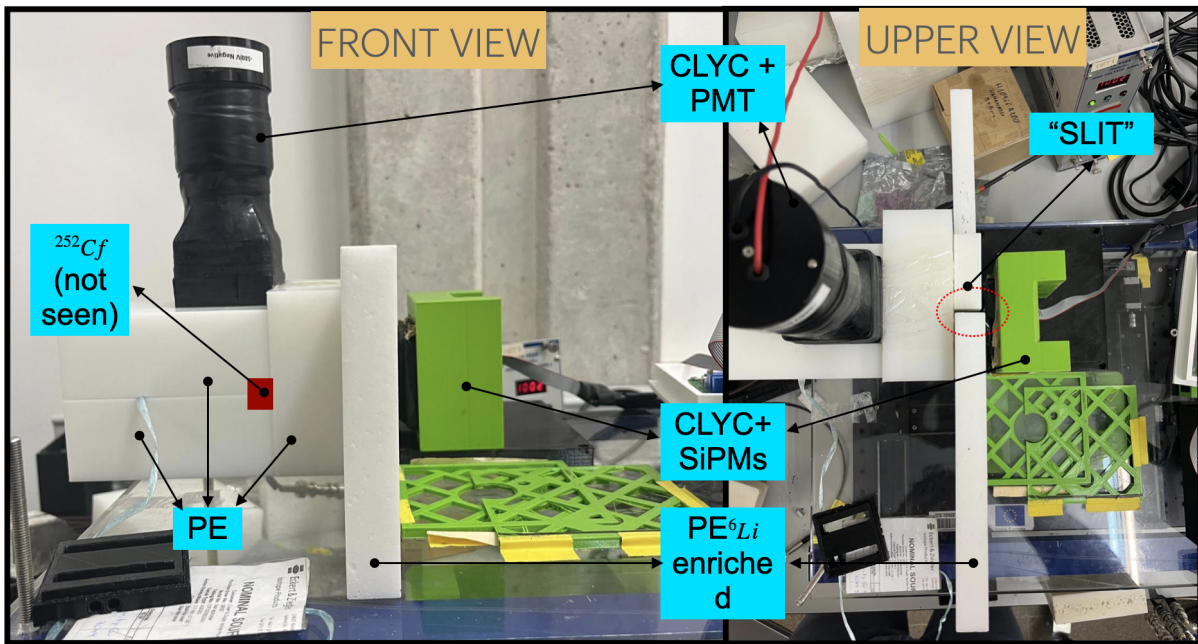


Figure 3.2.1: Experimental setup for neutron radiation

In this setup, a source of ^{252}Cf was used, indicated by a red square, and surrounded by polyethylene. ^{252}Cf decays mainly through alpha decay and spontaneous fission, with about 3% decaying by spontaneous fission. This process splits the nucleus into two lighter nuclei, releasing energy and several neutrons:



To better understand the setup, Figure 3.2.2 illustrates the experimental configuration. The neutrons' fission spectrum ranges from thermal to fast neutrons. To thermalize them, a 5mm piece of polyethylene (PE) was used in front of and covering the source. Next to this covering, a slab made of PE enriched with 95% ^6Li was placed. This slab has an **slit**

in the middle through which thermal neutrons can reach the detector, as seen in the upper view. Essentially, the measurements are expected to show an interaction pattern in the crystal that represents this opening.

The readout is the same as in the gamma irradiation configuration, with the only difference being that in this case, the SUM channel has been duplicated into two channels, each with specific parameters in the CAEN DAC to enhance the energy resolution and PSD discrimination.

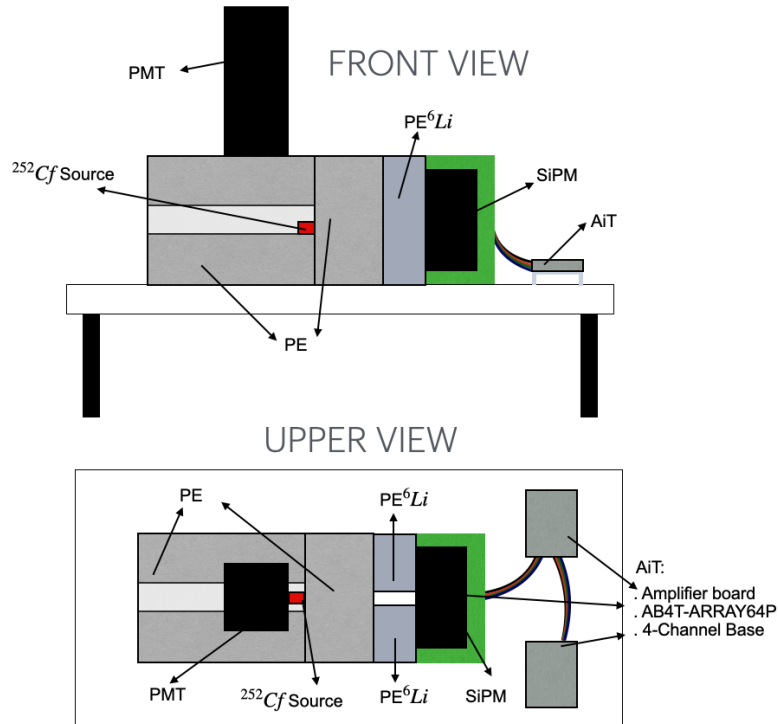


Figure 3.2.2: Illustrative scheme of the experimental setup

Results Gamma Irradiation

4.1 Gamma-Ray Event Selection

The first measurement was done centering the center of the collimator hole with the center of the CLYC crystal. To do so, the movable table was shift approximately to the center through visual inspection. The time of measurement was 12 hours. Then, the data was filtered to remove non-coincidence events. The two 511 KeV annihilation gamma rays will reach the CLYC+PTM and CLYC+SIMPs detectors respectively within a time window. This allows us to set a condition on the timestamp recorded by the CAEN DAC for the data. Fig. 4.1.2 shows the remaining data after filtering by selecting events within a time windows of 100 ns.

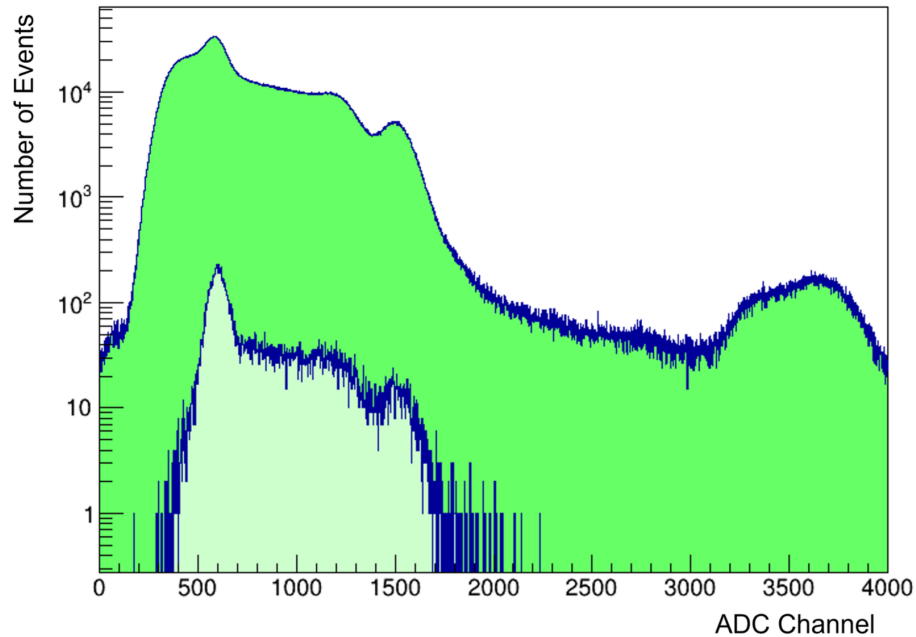


Figure 4.1.1: CAMBIAR IMAGEN POR LA QUE YO HICE

The 511 KeV photo-peak is around 500 channels (known from previous calibration). It is seen that the filtered data enhances the determination of the photo-peak area. There are events at higher and lower energies of the photo-peak since there are other coincident events within the time window apart from the two 511 KeV gamma rays. These can be removed by filtering in energy. In Fig. ??, the coincident events are shown along with the energy cut. Thus, these events will create the interaction position.

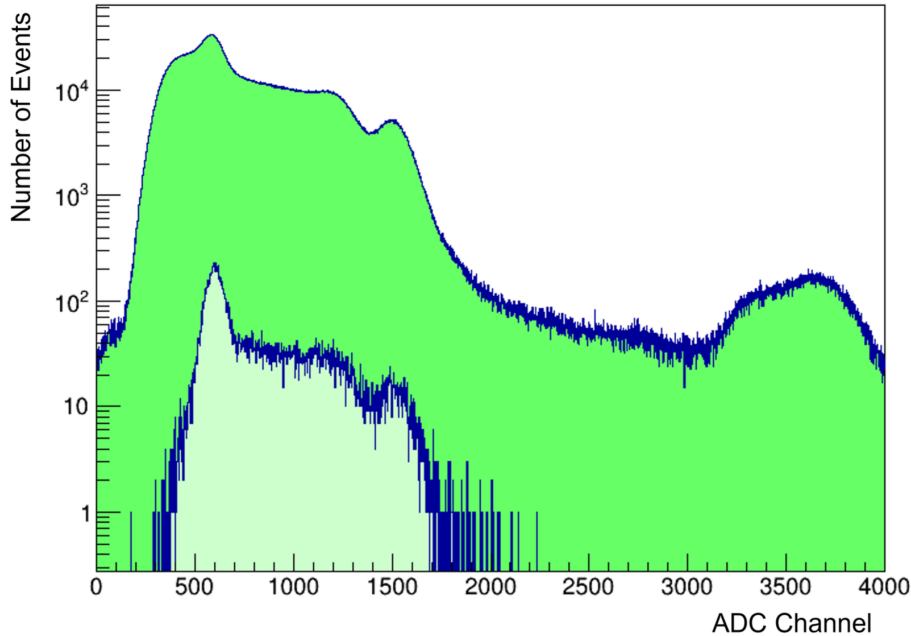


Figure 4.1.2: CAMBIAR IMAGEN POR LA QUE HICE YO PERO DEL CANAL 0 SOLAMENTE

4.2 Interaction Position Reconstruction

Once events filtering is done, it's possible to reconstruction the position of interaction by applying eq. ???. Fig. 4.2.1 shows the reconstruction position when the collimator is center with the center of the CLYC crystal + SiPM array.

Clearly there is a dispersion pattern of interaction pixels surrounding the center of the crystal, position at which an increase in the amount of counts is seen. In Figs. ???, projection to X and Y plane is depicted. To identify the centroid of the distribution along with the dispersion, Gaussian functions has been fitted in each projection.

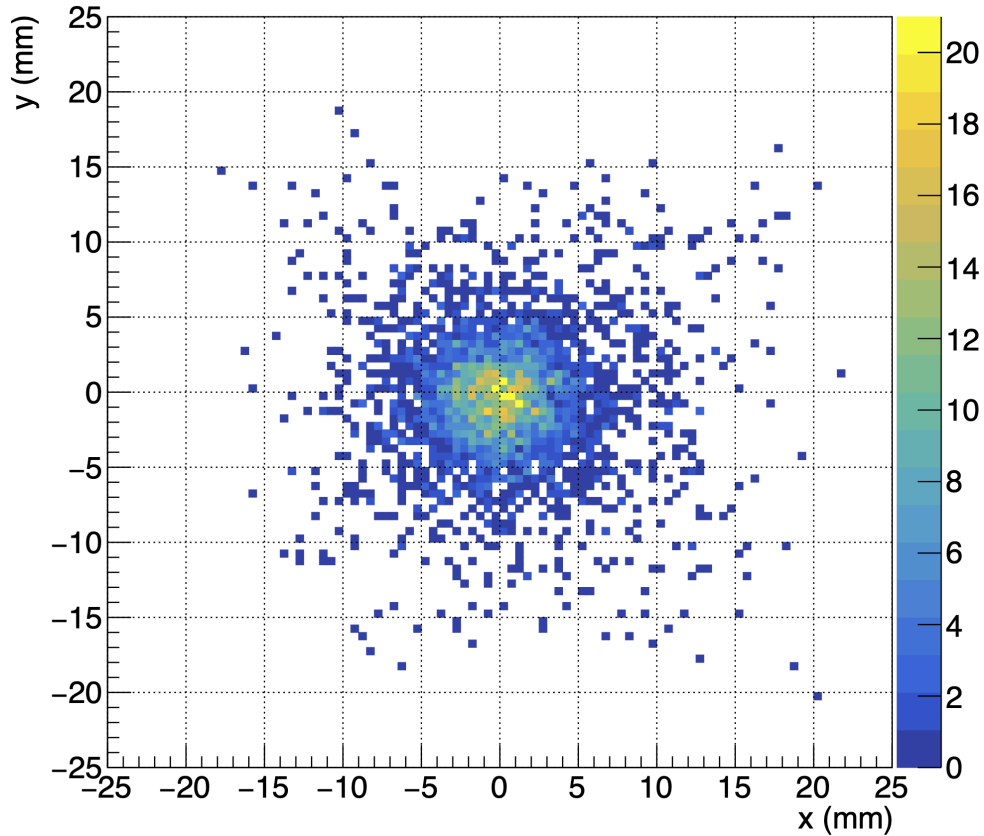


Figure 4.2.1: Caption for the energy-filtering image

In this measurement, the mean of both profiles are near 0 mm and the standard deviations around to 3 mm. This pattern truly reflect the effect of the collimator system centered in the center of the CLYC crystal.

Same proceed was carried on for different positions between the collimator center and the CLYC crystal. These positions comprehend different points throughout the crystal surface. For better understanding, only six positions are displayed in Fig. ?? along with the projections to X and Y planes with their respective Gaussian fits underneath. Each position varies respect to the previous one in a displacement of the collimator center of 5 mm in X and Y, meaning that they are along one diagonal of the crystal. The dotted black line is upon this diagonal for visual aid. The red lines represent the cuts to get the projections.

First of all, there is a clear tendency for the distribution of interaction points to follow the diagonal, showing the effectiveness of the experimental setup. However, it is observed that in the two extreme positions ($x = -20$ mm, $y = -20$ mm) and ($x = -15$ mm, $y =$

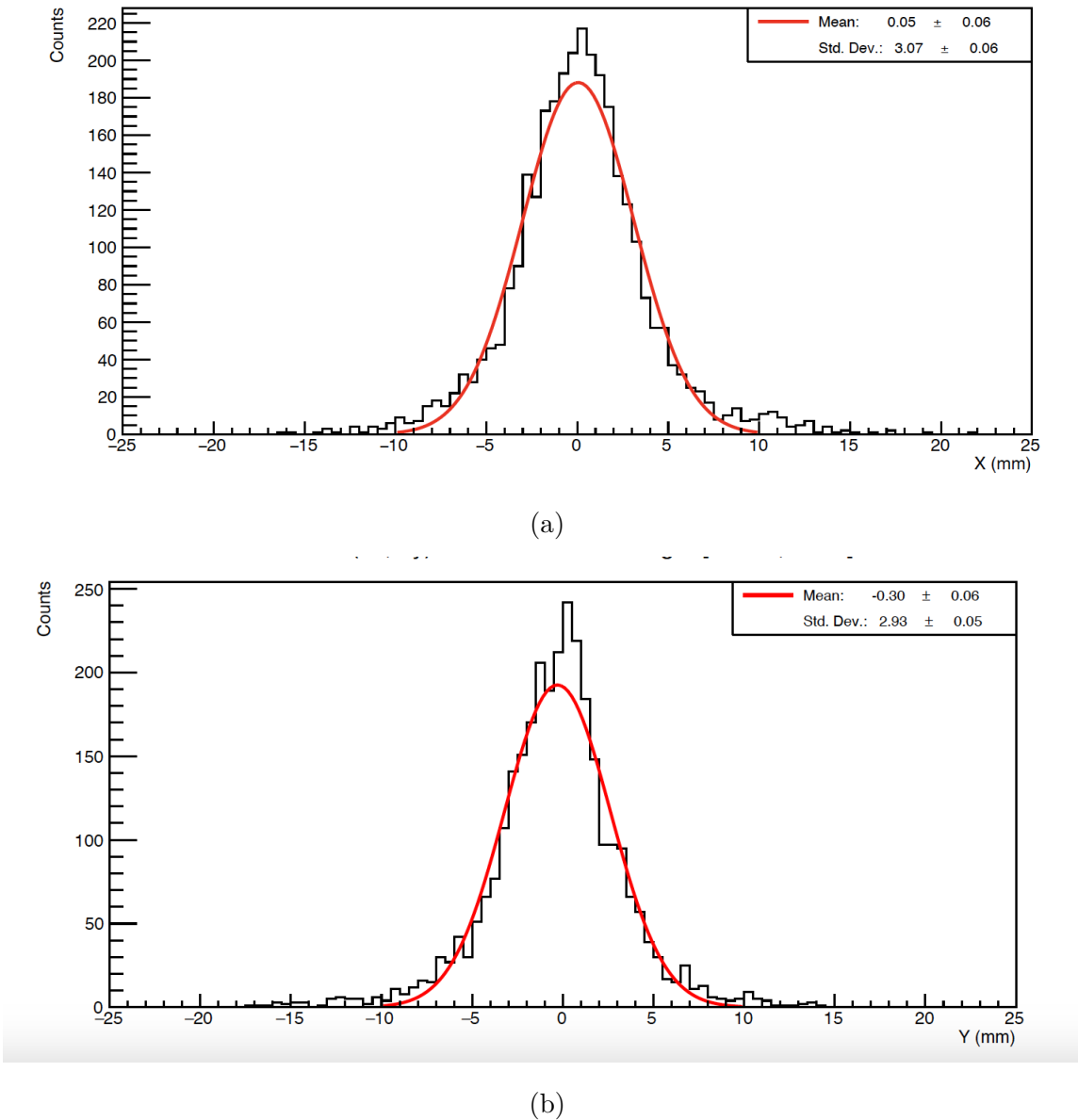


Figure 4.2.2: Título de la figura que incluye ambas subfiguras

-15 mm), the centroids are shifted toward the center of the crystal rather than being near the position of the collimator, as is the case for the other positions. This effect is called the "Linearity" of the crystal when reconstructing the position and is a well-known phenomenon that will be characterized. It occurs because of the internal reflecting material on the border of the crystal, which is used to improve the collection of light ??.

In regard to dispersion, the standard deviation values are around 3 mm. These values represent not only the resolution capability of the CLYC+SiPM array and AiT read-out electronics but also the conditions of the experimental setup, including the spatial con-

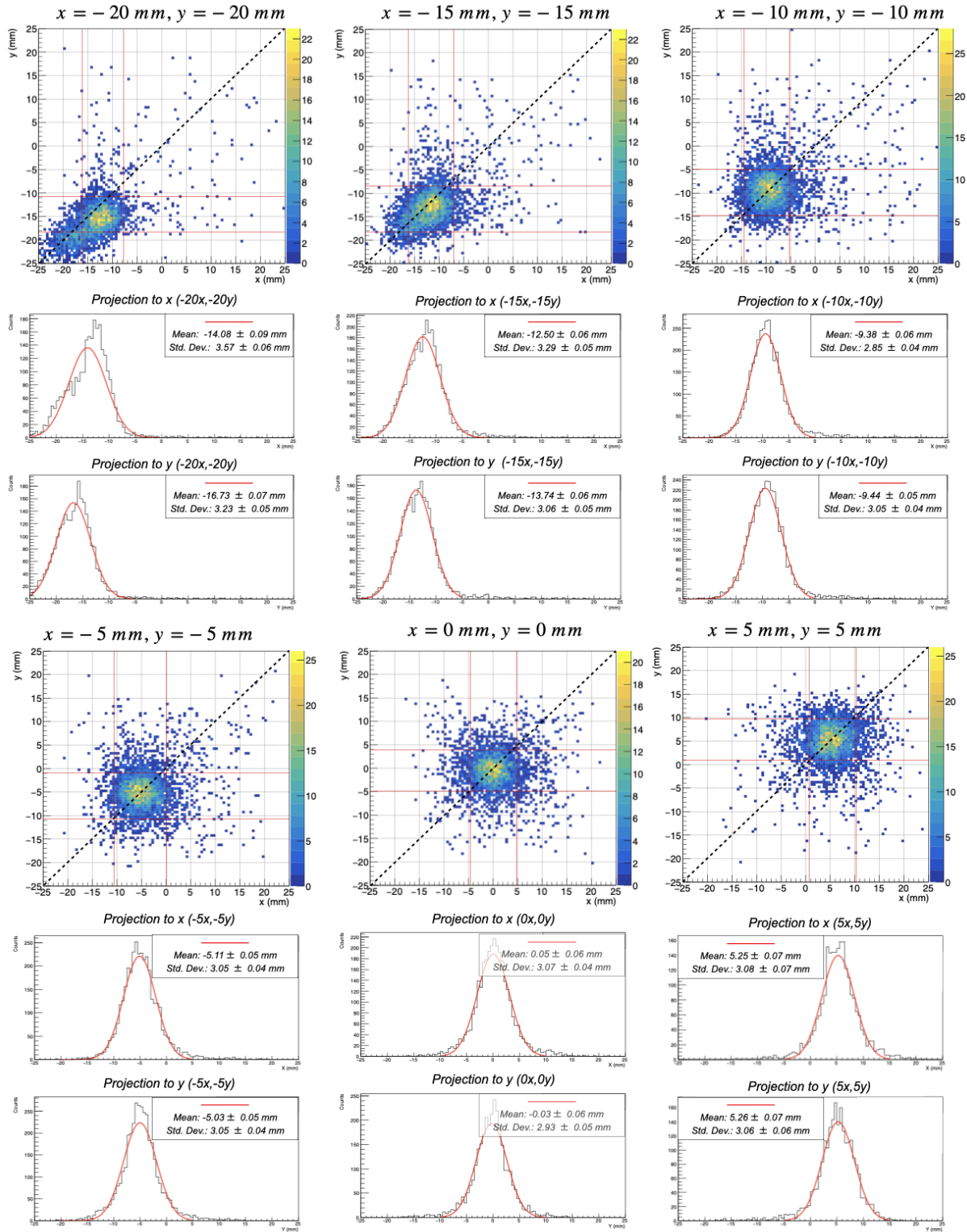


Figure 4.2.3: Caption

figuration, the collimation system, the material surrounding the main setup, background radiation, etc.

To isolate CLYC+SiPM uncertainties, the use of GEANT4 will be necessary.

4.3 GEANT4 Simulations

GEANT4 is a simulation platform developed by CERN, used to model the interaction of particles with matter. It allows for the construction of detailed geometric models and the application of precise physical models to study particle behavior in various experimental contexts. This tool is essential in particle physics, medicine, and other scientific fields for performing detailed and accurate simulations.

In order to understand the distribution dispersion related to the experimental setup, isolated from the CLYC crystal and subsequent SiPM array and AiT electronic readout, the identical configuration was modeled using GEANT4, as seen in Fig. 4.3.1. The material of each component has been precisely modeled to reproduce reality as closely as possible. However, the physics behind the production of light collected by the SiPMs is not of interest for the purposes of this development. Hence, the simulation focuses on understanding the dispersion of the 511 KeV gamma rays when they reach the detector. The decays of ^{22}Na have been modeled along with the positron-electron annihilation that gives rise to the two 511 KeV gamma rays. The CLYC scintillator in the upper part fulfills the same criteria as in the real setup, to measure in coincidence with the one at the bottom.

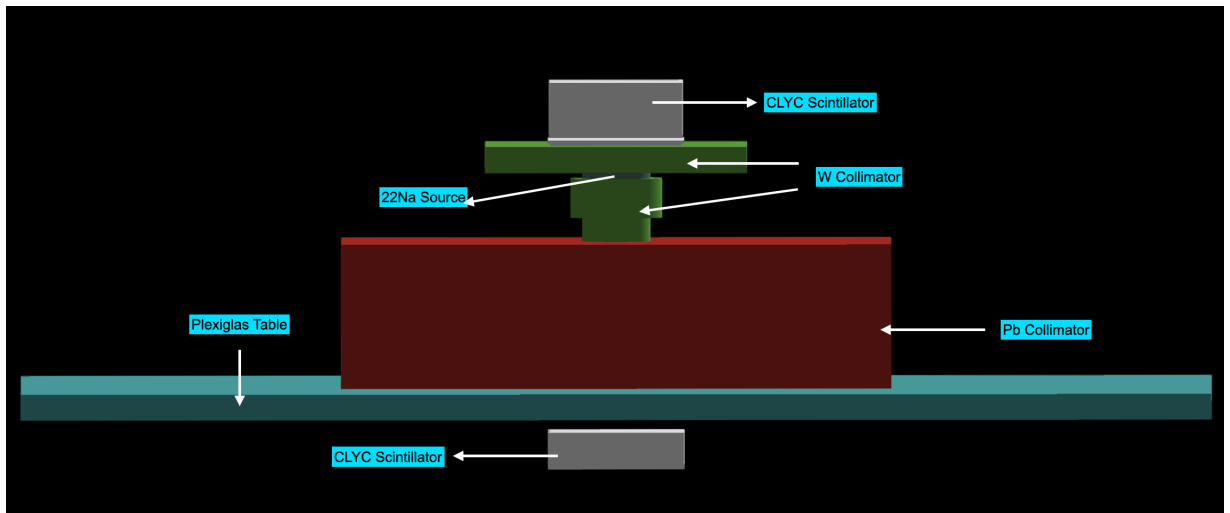


Figure 4.3.1: GEANT4 simulation setup

Figure 4.3.2 shows the interaction points simulated through GEANT4 when the collimator

is centered in the middle of the crystal. Figure 4.3.3 shows the projection onto the X and Y planes. Apart from the centroid around 0, the important aspect here is that the dispersion is now smaller compared to the dispersion obtained in the previous measurements, which is an expected result given that the simulation is not considering the production of light in the CLYC scintillator nor its collection by the SiPMs and subsequent signal processing. This procedure was repeated for all the positions measured previously.

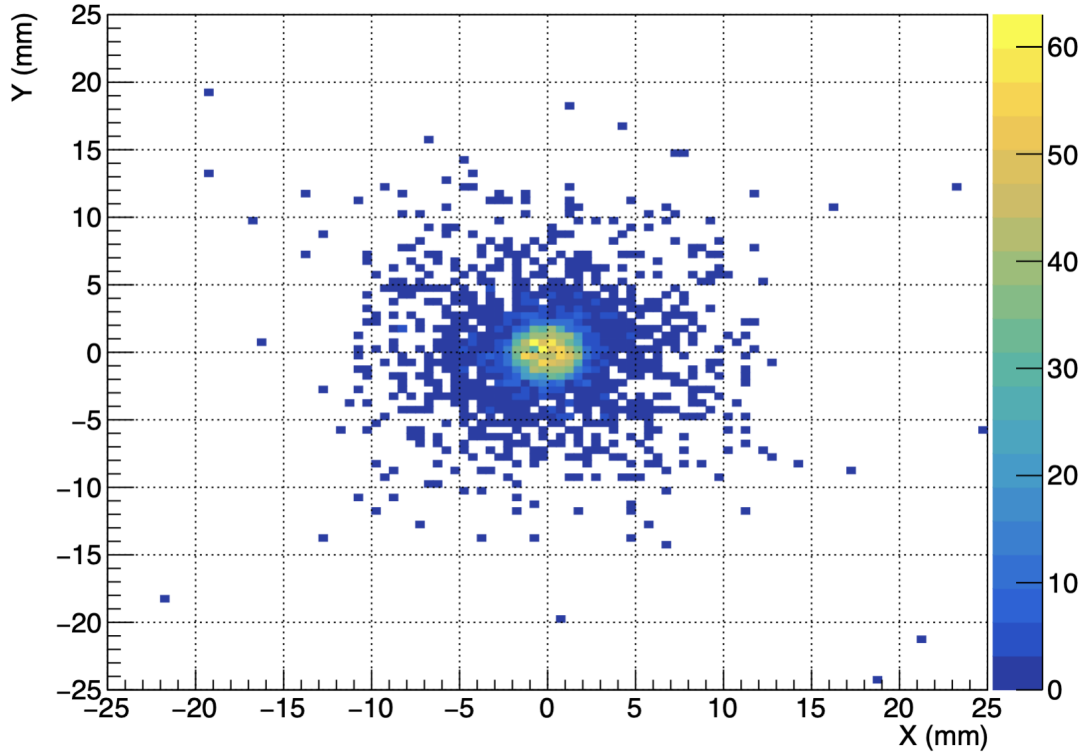


Figure 4.3.2: GEANT4

Then, it is now possible to understand the distribution dispersion related to the CLYC crystal and subsequent SiPM array and AiT electronic readout, denoted as $\sigma_{\text{CLYC+SiPM+AiT}}$, isolated from the distribution inherent to the experimental setup, which we will call σ_{SETUP} . To do so, it might be thought that the set CLYC + SiPM + AiT readout introduces an additional uncertainty $\sigma_{\text{CLYC+SiPM+AiT}}$ to the interaction position distributions obtained with GEANT4 simulations. This uncertainty is based on several factors such as the angular distribution of the emission light produced in the CLYC, the responses of the SiPMs, the energy resolution of the AiT readout, etc. It is assumed that $\sigma_{\text{CLYC+SiPM+AiT}}$ is normally distributed. Hence, this can be written as:

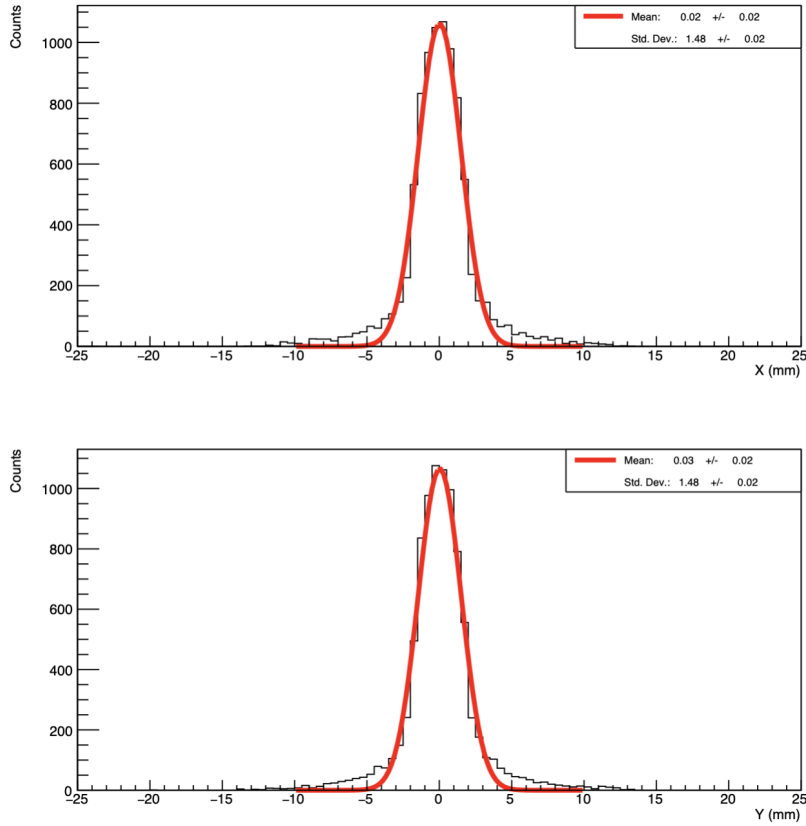


Figure 4.3.3: GEANT4 simulation projections onto the X and Y planes

$$f(\sigma_{\text{MEASURED}}, \mu) = g(\sigma_{\text{SETUP}}, \mu) \circledast \mathcal{N}(\sigma_{\text{CLYC+SiPM+AiT}}, \mu)$$

Where $f(\sigma_{\text{MEASURED}}, \mu)$ represents any interaction position distribution measured, $g(\sigma_{\text{SETUP}}, \mu)$ is any interaction position distribution simulated with GEANT4 and $\mathcal{N}(\sigma_{\text{CLYC+SiPM+AiT}}, \mu)$ represent the distribution associated to CLYC+SiPM+AiT readout when reconstructing the interaction position, assumed to be a Gaussian. The symbol \circledast represent a *Convolution* operation. Essentially, by convolving the function g with a Gaussian distribution \mathcal{N} , we obtain f . The key point for this development is the value of $\sigma_{\text{CLYC+SiPM+AiT}}$, which represents the spatial resolution of this system to determine the interaction position.

Figure 4.3.4 depicts the projections of Fig. 4.3.3 along with these projections convoluted with a Gaussian \mathcal{N} whose parameter is $\sigma_{\text{CLYC+SiPM+AiT}} = 2.30$.

The resulting projections from the convolution are then compared with the measurements performed in Fig. 4.3.5. If the results coincide, meaning the projections are similar, the

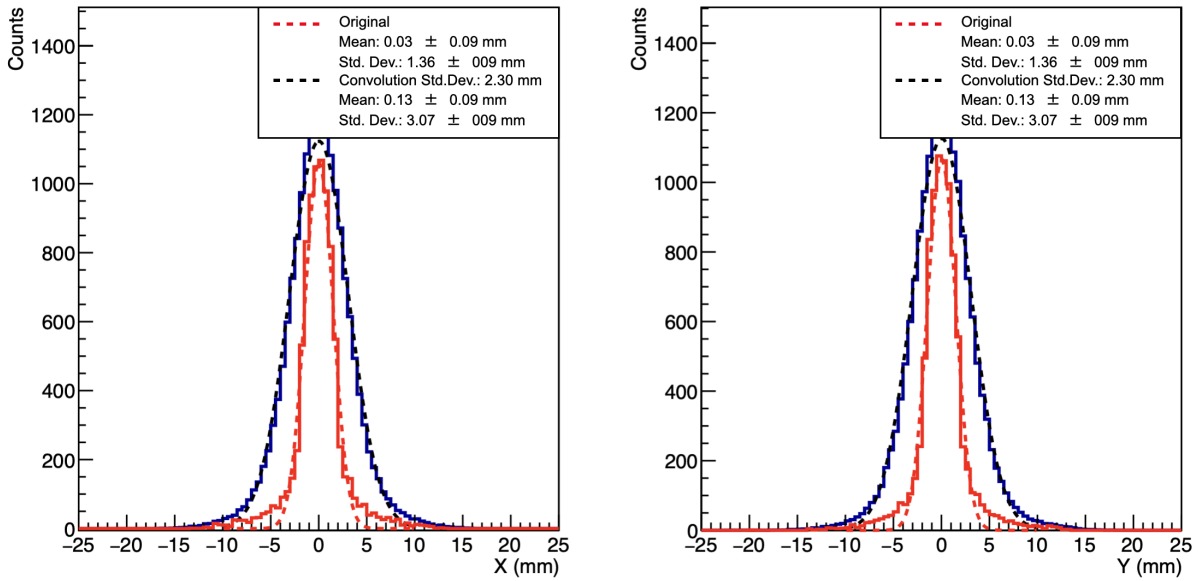


Figure 4.3.4: Projections of the GEANT4 simulation convoluted with a Gaussian distribution

Gaussian used for the convolution accurately represents the true dispersion of the CLYC + SiPM + AiT readout system. Consequently, the standard deviation of this Gaussian represents the resolution of this possible gamma detection system of GN-Vision when reconstructing the interaction position.

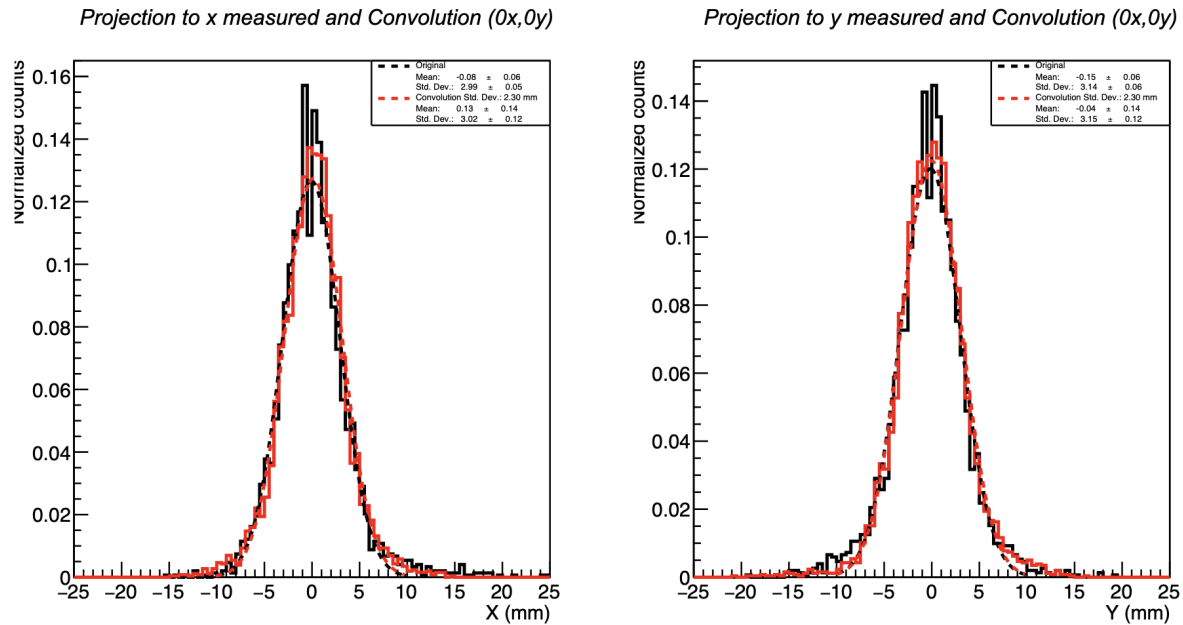


Figure 4.3.5: Comparison of the measured projections with the convoluted projections

By comparing the measured X and Y projections with the convoluted projections, it can be observed that the standard deviations of each are similar, indicating a match. Therefore, the Gaussian with a standard deviation of 2.30 mm represents the spatial resolution of the system for the central position of the crystal, without considering the experimental setup. Instead of the standard desviation, the spatial resolution is given by the FWHM (Full Width at Half Maximum), which for the case the collimator placed at the center of the crystal, the FWHM result to be 5.40 mm. This same procedure was repeated for all measured positions to obtain the FWHM of the projections onto X and Y without considering the experimental setup.

Fig. 4.3.6 depicts all the positions measured within the crystal. The reconstructed centroid is shown as the Full Width at Half Maximum (FWHM) of the projections onto the X and Y planes using the previous methodology. Different colors and/or symbols have been used to differentiate parts of the crystal where these positions have been measured. However, only the measurements with \blacktriangledown (along the diagonal) have been taken with a different configuration of the CAEN DAQ, which was not optimized for the best energy resolution.

In Table A.0.1 from Appendix A, the X centroid, Y centroid, and FWHM of all the measured positions are listed along with the positions at which the collimator was placed. These last are the X ideal position and Y ideal position, which ideally should match the positions of the centroids.

The FWHM obtained in these measurements is generally below 6 mm, which is notable considering the pixel size of the SiPM array is 6 mm x 6 mm. This demonstrates that the system can achieve a finer spatial resolution than the individual pixel size. Indeed, several points have FWHM values below 5 mm. Points of types "V" and some "D" and "AD" show FWHM in the range of 3.17925 mm to 5.41650 mm.

The points with the highest FWHM values correspond to those where the CAEN DAQ configuration was not optimized for the best energy resolution and are located at the edges of the crystal, where there is more compression. This lack of optimization and the higher compression at the crystal edges contribute to a higher FWHM. In particular, the two points marked with \blacktriangledown on the upper left corner (along the diagonal) show a FWHM higher of 6 mm due to these conditions.

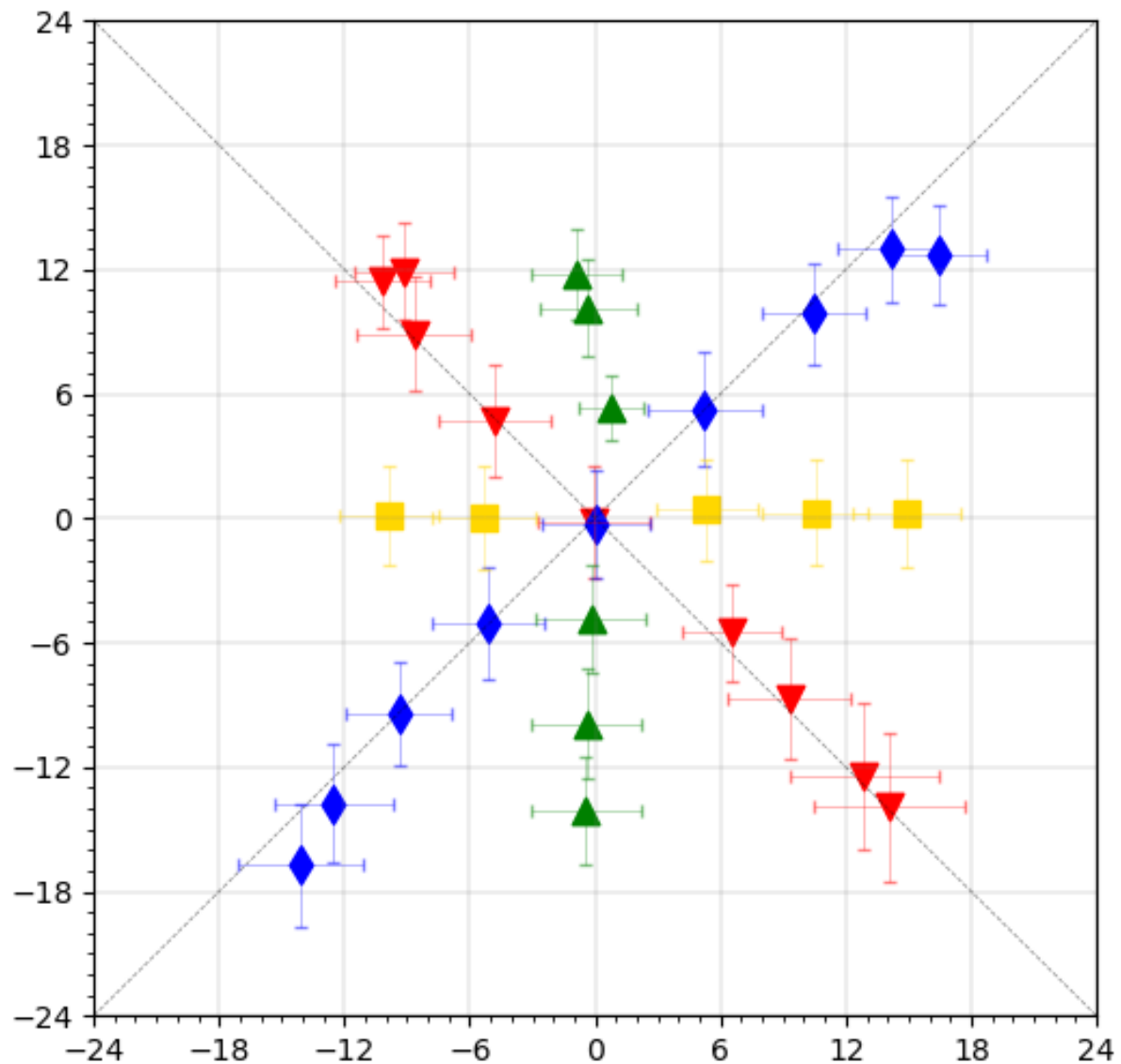


Figure 4.3.6: Positions measured within the crystal, with the reconstructed centroid shown as the FWHM of the projections onto X and Y planes. Different colors differentiate parts of the crystal.

To understand the loss of linearity in the reconstructed position within the CLYC crystal, Fig. 4.3.7 illustrates the ideally reconstructed X and Y components (determined by the collimator position) versus the actual reconstructed position (determined by the centroid position). It can be observed that linearity is maintained at the center of the crystal. However, as the reconstructed position moves further from the center, linearity starts to deteriorate. Beyond 15 mm, the compression effect becomes more significant, and almost no positions are reconstructed in this area. This does not imply that the crystal is

insensitive in these compressed areas. Instead, it indicates that the reconstructed position is shifted toward the center. To accurately reconstruct the interaction position in these regions, additional characterization of this effect is necessary.

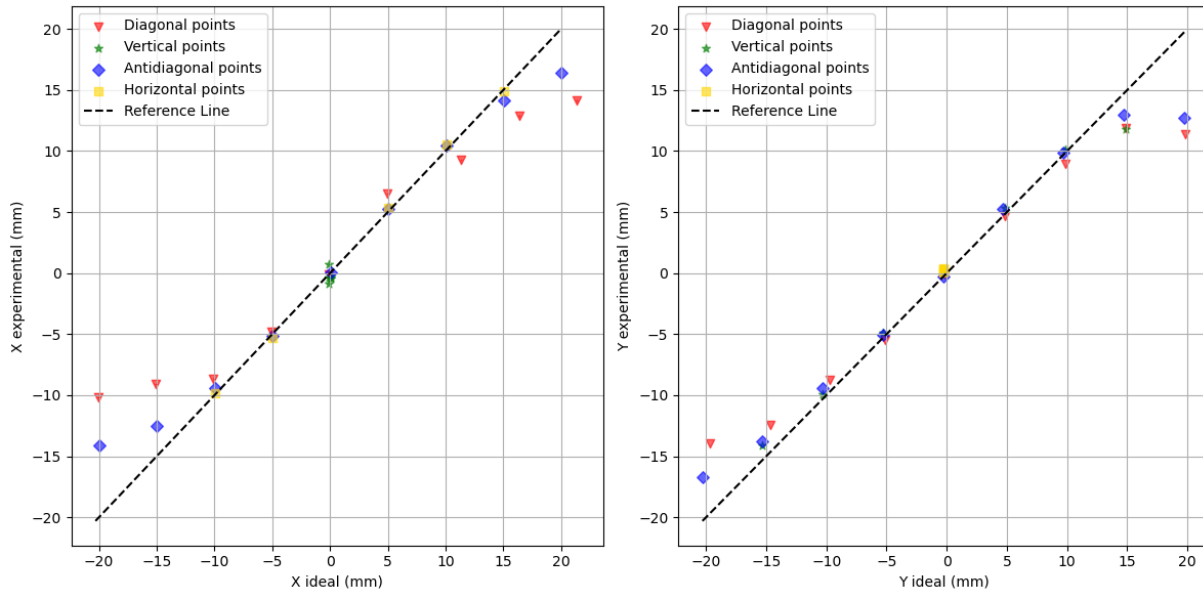
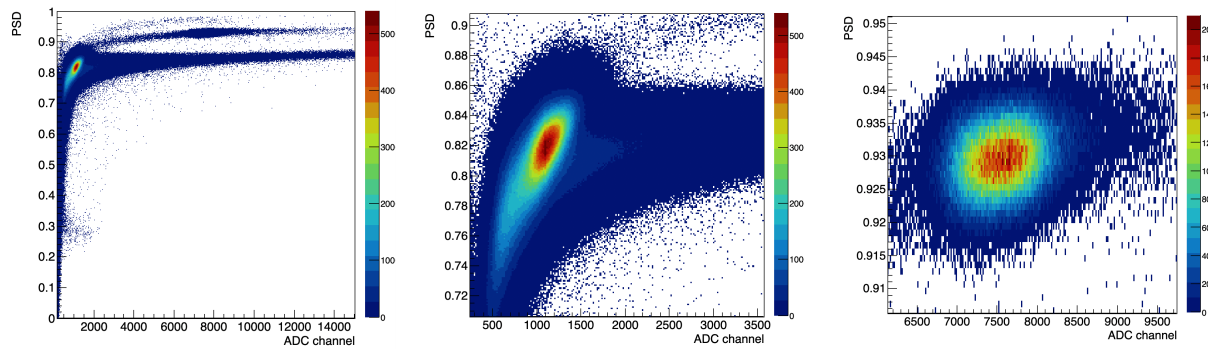


Figure 4.3.7: Comparison of ideally reconstructed X and Y components with the actual reconstructed position.

Results Neutron Irradiation

As said, the main objectives here are to verify the system's capability to distinguish between gamma and neutron radiation. To start with, Pulse Shape Discrimination (PSD) vs Energy (ADC channels) is presented for the experimental setup shown in ???. As explained before, the DAQ system has been configured to enhance the energy resolution and the PSD in different channels. The configuration of each channel can be found in Appendix B.

Figure 5.0.1 presents the PSD vs Energy when the DAQ parameters have been configured to promote the best PSD outcomes but not for energy. The PSD for the whole energy spectra is showed in Fig. (a), a zoom on the gamma events in Fig. (b), and a zoom on the neutron events in Fig. (c).



(a) PSD for the whole energy (b) Zoom on the gamma events (c) Zoom on the neutron events

Figure 5.0.1: PSD vs Energy with DAQ parameters optimized for PSD but not for energy.

Figure 5.0.2 presents the optimized PSD and Energy by combining both optimized channels. All events at all energies are showed in Fig. (a), only gamma events in Fig. (b), and only neutron events in Fig. (c).

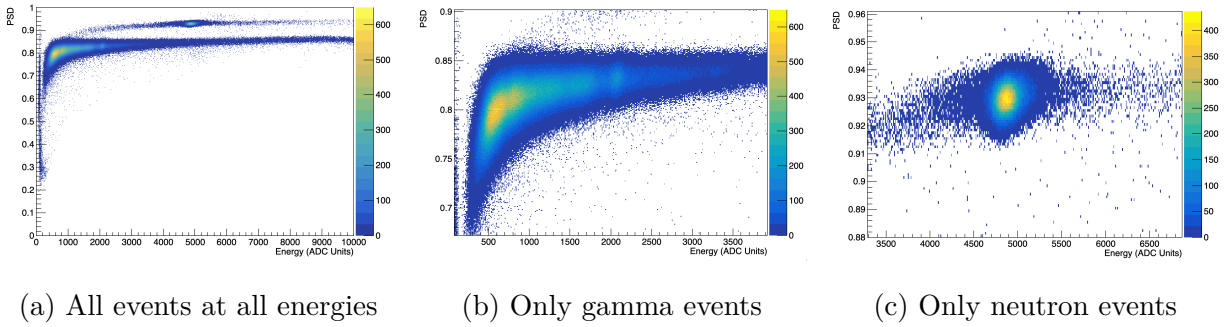


Figure 5.0.2: PSD vs Energy obtained by combining both optimized Energy and PSD channels.

5.1 Figure of Merit for PSD Evaluation

To evaluate the Pulse Shape Discrimination (PSD) capability, we define a Figure of Merit (FOM):

$$\text{FOM} = \frac{|\mu_n - \mu_\gamma|}{\text{FWHM}_\gamma + \text{FWHM}_n} \quad (5.1)$$

where:

- μ_γ and μ_n are the centroids of the Gaussian fits for gamma rays and neutrons, respectively.
- FWHM_γ and FWHM_n are the Full Widths at Half Maximum of the Gaussian fits for gamma rays and neutrons, respectively.

This FOM essentially measures the separation between the centroids of the two distributions (gamma and neutron) relative to their widths. A higher FOM indicates better discrimination between the two types of radiation. An FOM of 1 implies that the distance between the centroids of the gamma and neutron distributions is equal to the sum of their FWHMs. This means that the two distributions are just touching each other and are barely separable. In practical terms, a $\text{FOM} > 1$ implies that the distributions are well separated, providing excellent discrimination between gamma rays and neutrons.

In Fig. 5.1.1 , a projection onto the PSD axis with the PSD values versus energy (in the not optimized energy scenario) was done. Gaussian functions were then fitted to the

gamma and neutron distributions to determine their respective centroids (μ_γ and μ_n) and Full Widths at Half Maximum (FWHM). Hence, FOM accurately calculated.

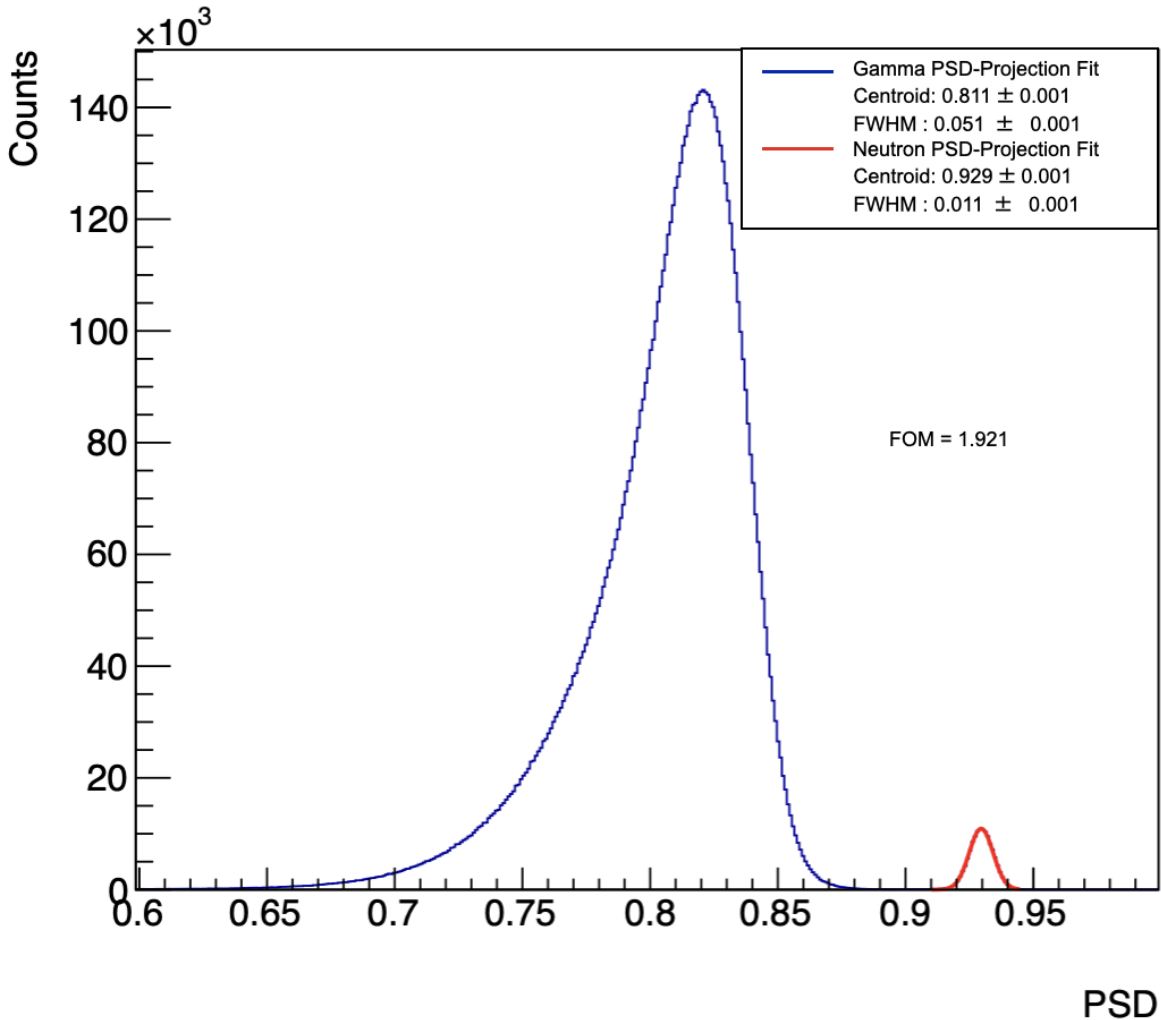


Figure 5.1.1: Projection onto PSD axis and Gaussian fits of Gamma and Neutron distributions. The centroids (μ_γ, μ_n) and the FWHMs are shown along with the FOM, being equal to 1.921.

Then, by filtering events in PSD and Energy, it's possible to reconstruct the interaction position of thermal neutrons in the crystal. Fig. 5.1.2 shows the interaction position created from the experimental setup of Fig. ??.

It's observed that there is a clear increase in the number of counts in the center along a horizontal direction. This is likely due to the unshielded part provided by the slit. However, since the ^{252}Cf source emits fast neutrons as well, the PE ^6Li isn't efficient against

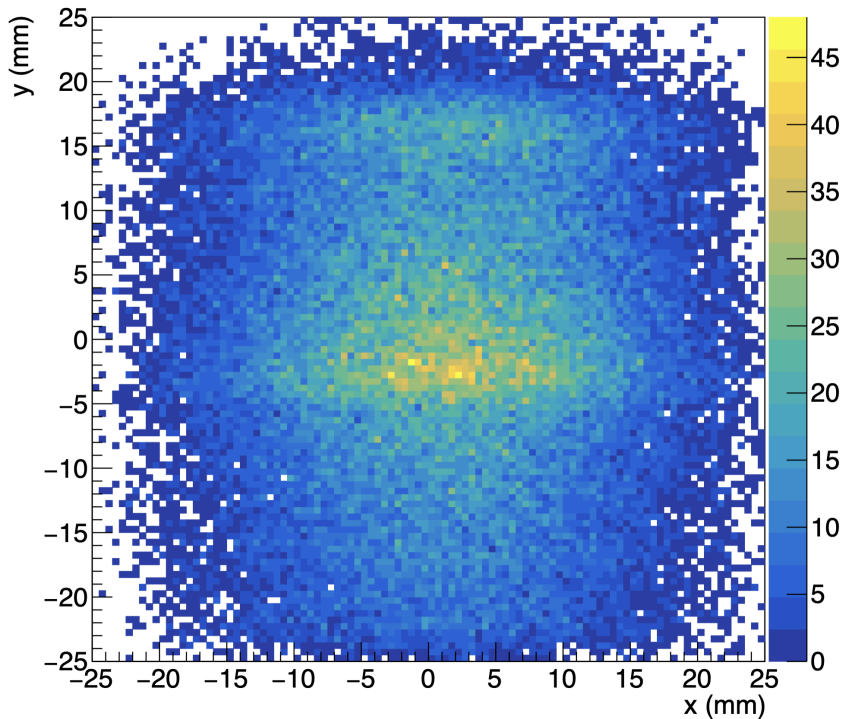


Figure 5.1.2: Interaction position of thermal neutrons with the slit open

these neutrons. Therefore, there are interaction positions throughout the entire area of the crystal. Fig. 5.1.3 presents the reconstruction of the interaction position in the crystal but now with the slit closed. The PE⁶Li has been placed to close the aperture previously formed. The intention is to measure the interaction position during the same amount of time as the previous measurement in order to subtract this measurement from the one with the slit open. By doing so, it's possible to effectively subtract the background from the measurement.

Figure 5.1.4 shows the difference between the measurement with the slit open and the background measurement with the slit closed. This effectively highlights the interaction positions due to the unshielded part, providing a clearer representation of the thermal neutron interactions.

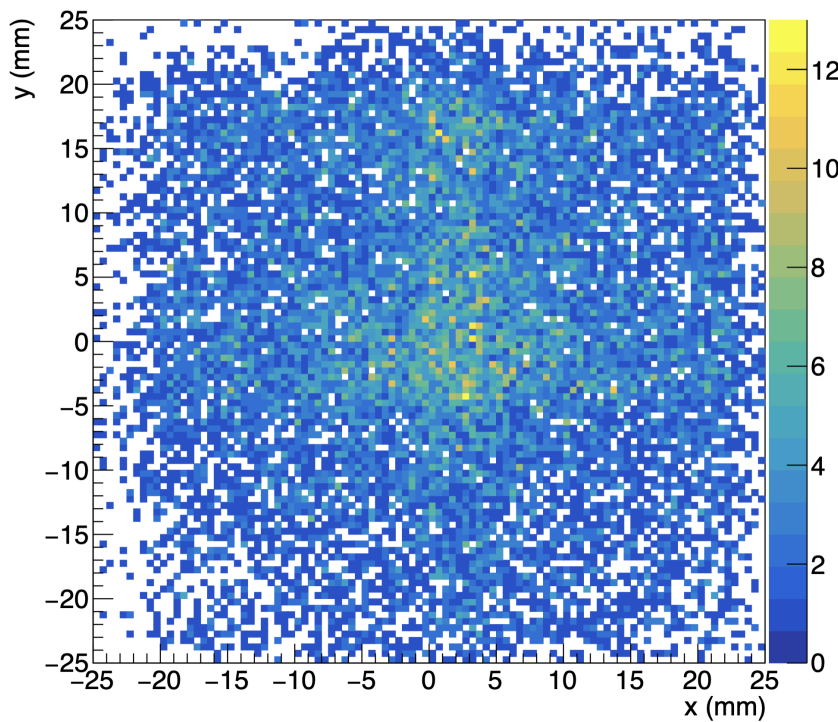


Figure 5.1.3: Interaction position of thermal neutrons with the slit closed

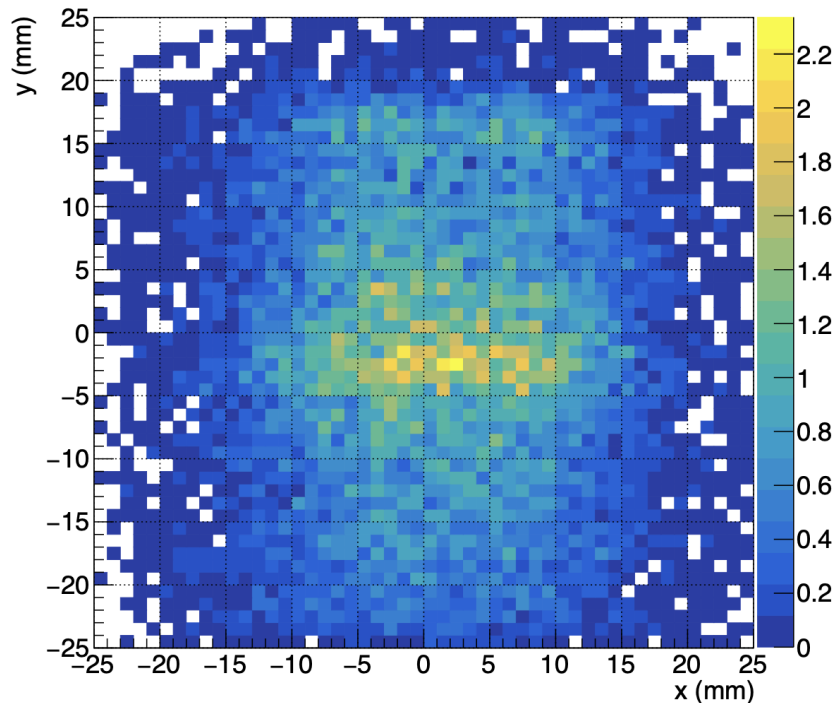


Figure 5.1.4: Difference between the measurement with the slit open and the background measurement with the slit closed

Performance of GN-VISION

This chapter focuses on the study of the performance of GN-VISION through simulations of GEANT4. The geometry model implemented in GEANT4 is shown in Fig. 6.0.1. In this simulation, the critical parameters are shown in the design of the neutron collimator: diameter (D) = 2.5 mm, thickness (T) = 20 mm, and focal distance (F) = 40 mm. An additional parameter of relevance for the Compton imaging technique is the distance between the two detection planes, here defined as 200 mm. All these parameters have been set with some of the values studied in ?? for future comparison and further analysis.

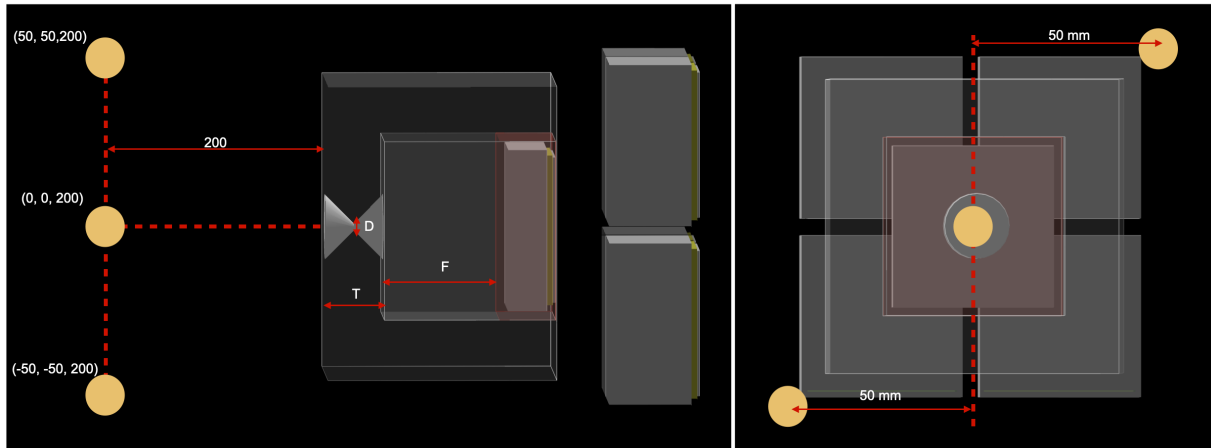


Figure 6.0.1: Geometry model implemented in GEANT4 for GN-VISION

The emissions of neutrons and gamma radiation have been modeled in separate simulations. For neutrons, the simulation considers three isotropic point-like sources of neutrons located at 20 cm from the collimator and separated from each other by 5 cm in the X and Y axes, as sketched in Fig. 6.0.1, with an energy of 0.025 eV, emitted isotropically. A total of 10^8 neutrons were randomly generated from each of the sources. Regarding gamma radiation, the three neutron sources were changed to emit 511 KeV gamma rays (since the spatial resolution obtained earlier was measured at this energy). In this case, only

the gamma ray has been simulated, not the decay of ^{22}Na with its subsequent positron annihilation. The emission in this case is also isotropic.

To study the impact of the spatial resolution on the CLYC crystal (scatter), interaction positions (output data of the simulations) were convoluted with a Gaussian Distribution with a standard deviation of 2 mm, both for neutron and gamma radiation. Additionally, interaction positions were shifted by multiplying them by a factor to account for spatial linearity, as shown in Figs. 6.0.2 and 6.0.3. This factor represents the ratio between the centroid measured in the gamma-irradiation experimental setup and the ideal centroid (given by the position of the collimator in the gamma setup as well).

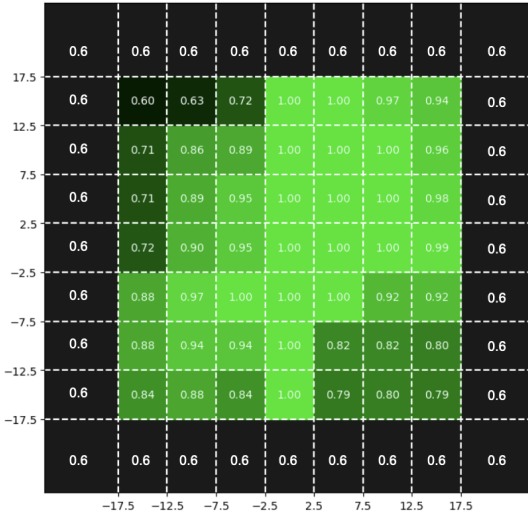


Figure 6.0.2: Linearity in the X direction

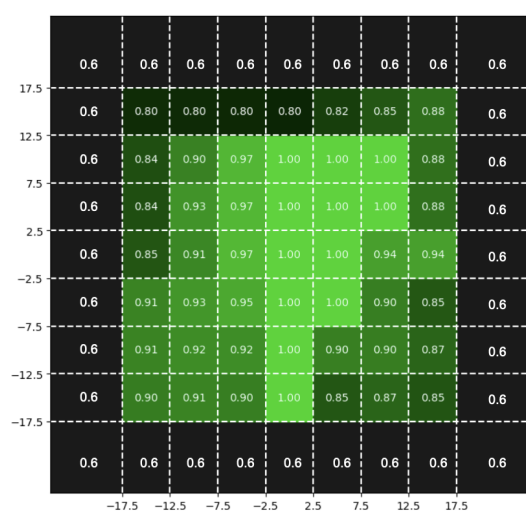


Figure 6.0.3: Linearity in the Y direction

6.1 Gamma-ray Simulation

The result for gamma-ray imaging when no spatial resolution nor compression effect is present, in order to contrast this result when there are spatial effects, is shown in Fig. 6.1.1. The projection onto the X and Y axes is presented in Figs. 6.1.2 and 6.1.3.

For gamma-ray imaging with experimental spatial effects, Fig. 6.1.4 and Fig. ?? show how spatial resolution and compression effects impact the imaging quality.

Clearly, there is a broadening effect on the distribution of each source (almost double in the distribution center in the middle and more than double in the other two sources). However,

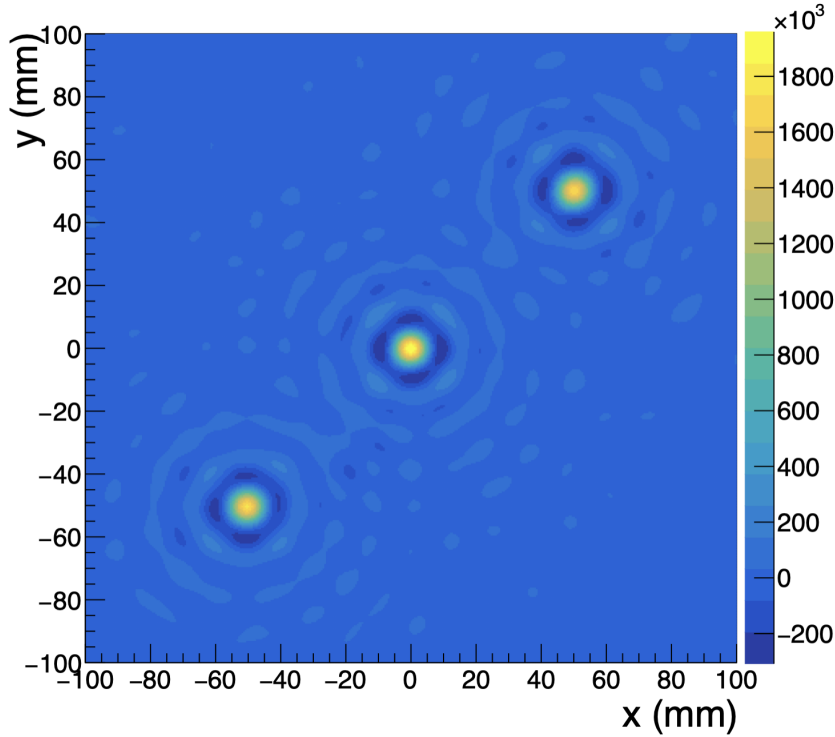


Figure 6.1.1: Imaging results for gamma radiation. No experimental spatial effects.

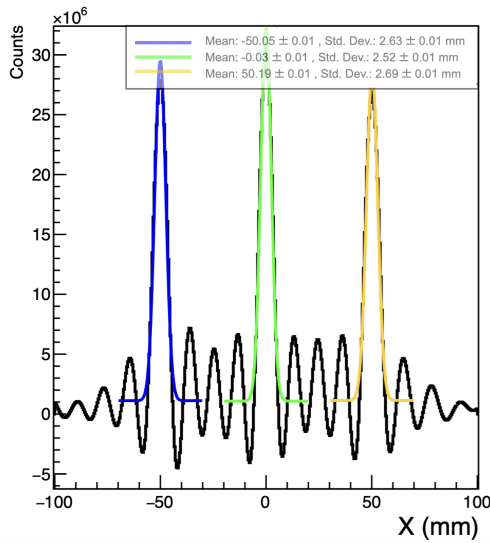


Figure 6.1.2: Compton imaging projection in the X direction. No experimental spatial effects.

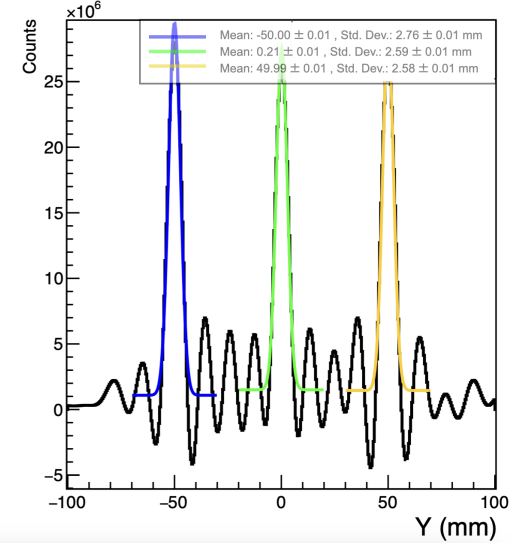


Figure 6.1.3: Compton imaging projection in the Y direction. No experimental spatial effects.

the centroids of the sources do not change much with these spatial effects, maintaining the values of the position of the source within the error. What does increase is the background

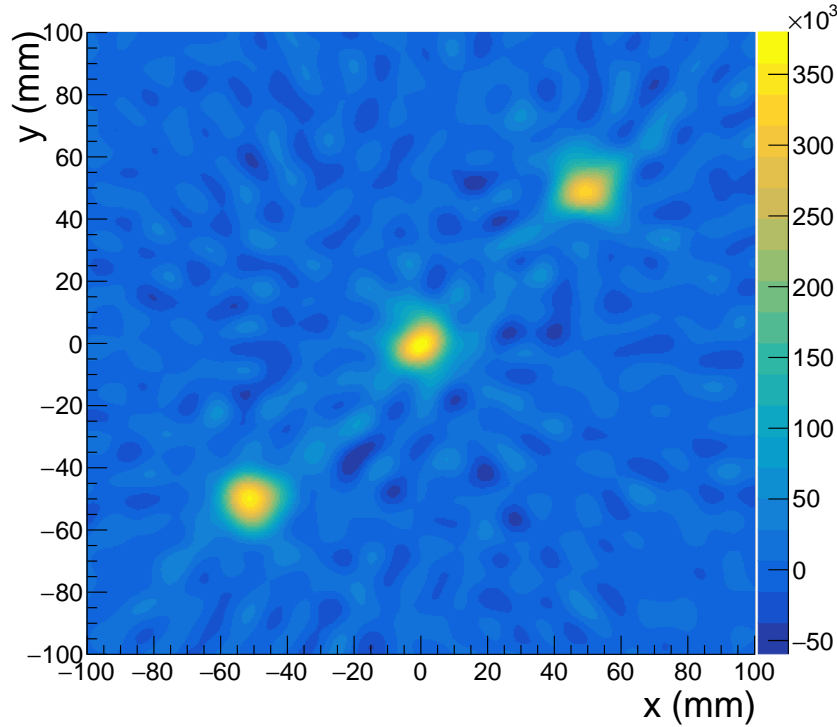


Figure 6.1.4: Imaging results for gamma radiation with experimental spatial effects

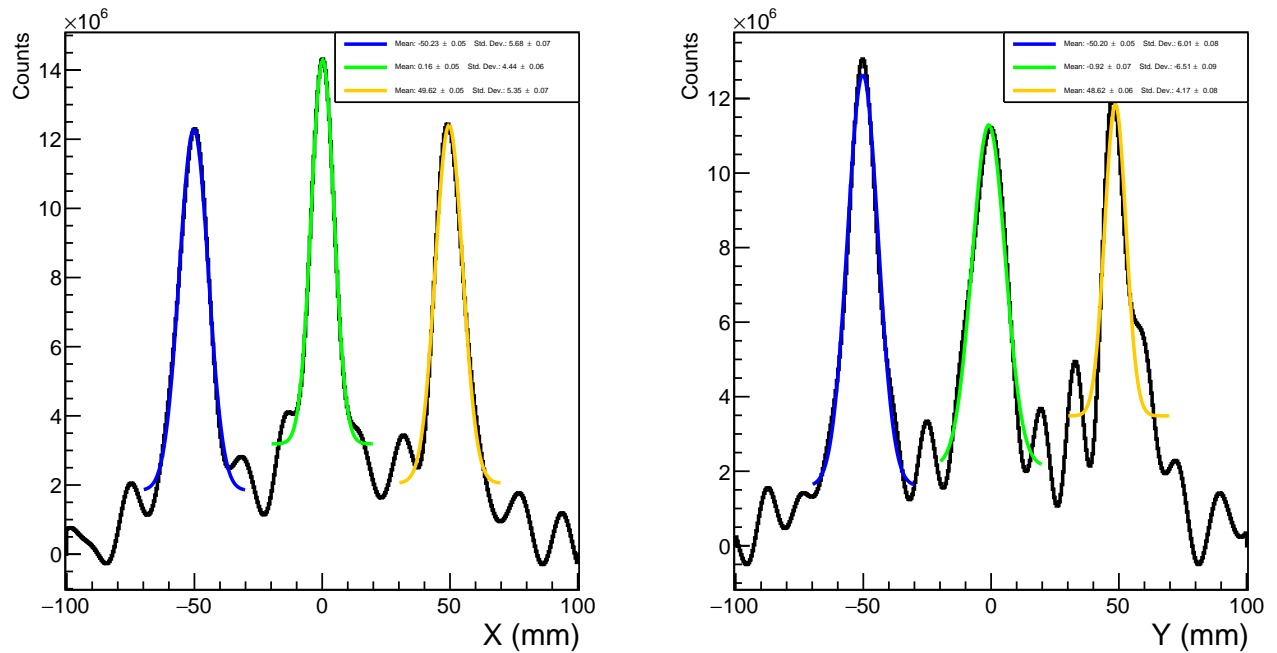


Figure 6.1.5: Projections with experimental spatial effects

of the image, making the image have less contrast compared to the case without the spatial effects. .

6.2 Neutron Simulation

The results for neutron imaging follow a similar approach as the gamma-ray simulations. Again, the interaction positions were convoluted with a Gaussian Distribution with a standard deviation of 2 mm and shifted by multiplying by the same matrix of Figs 6.0.2 and 6.0.3.

The result for neutron imaging without spatial resolution or compression effects is presented in Fig. 6.2.1. The projections onto the X and Y axes are shown in Figs. 6.2.5 and 6.2.6.

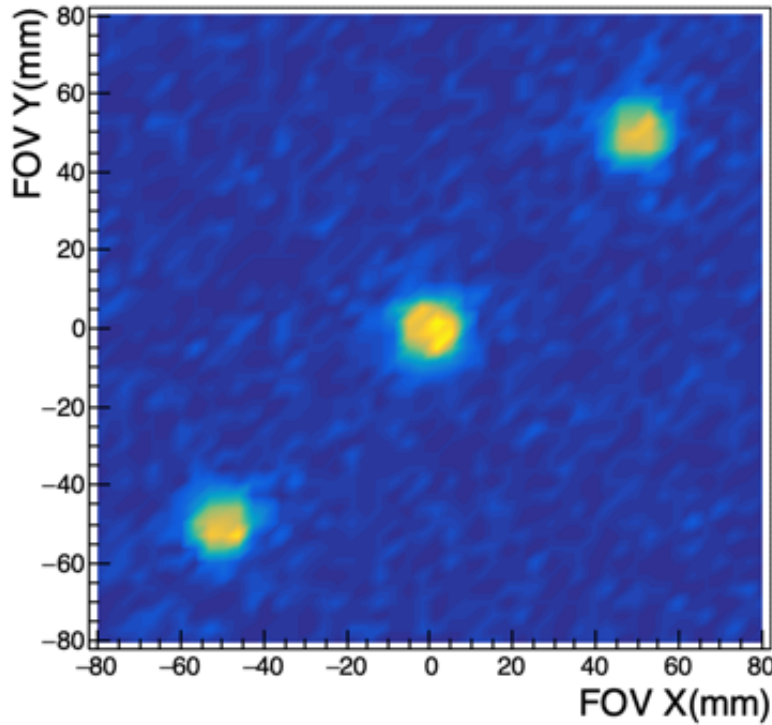
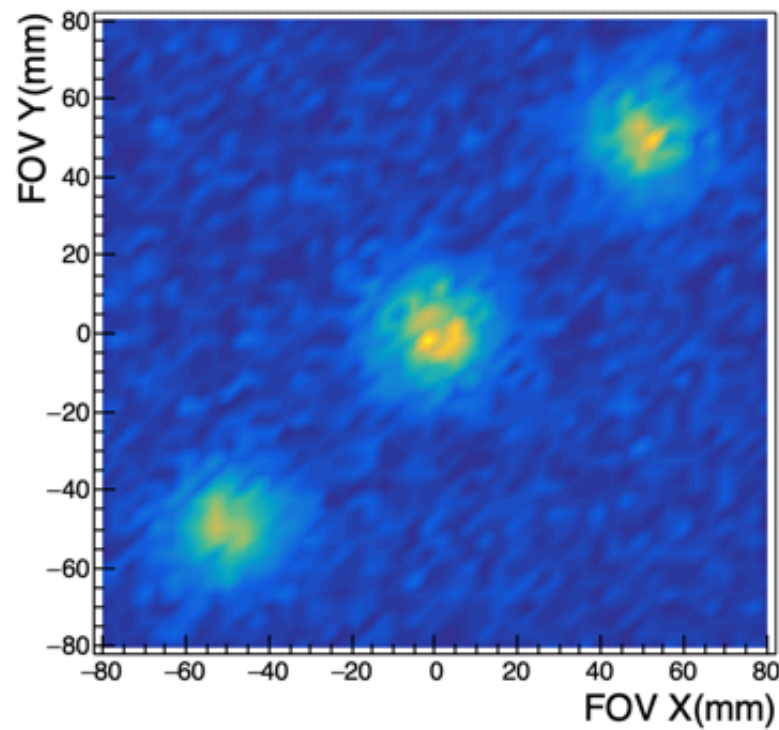
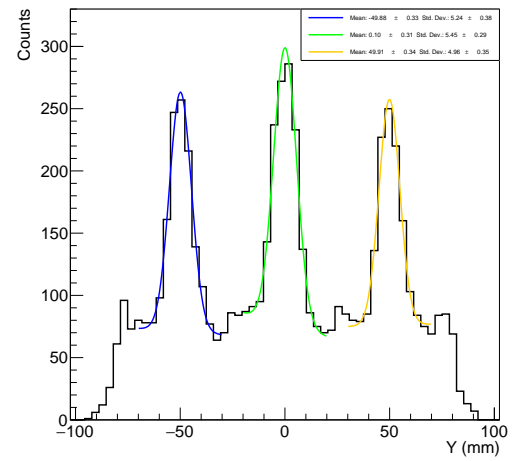
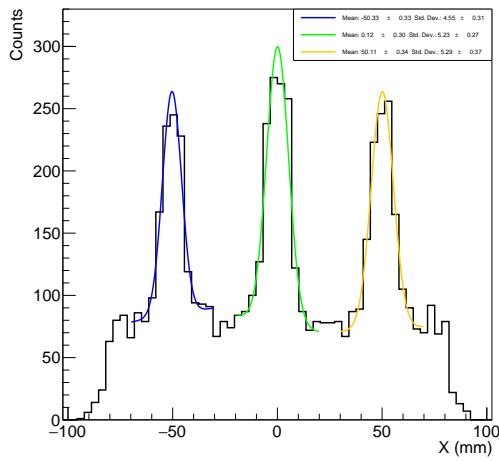


Figure 6.2.1: Imaging results for neutron radiation. No experimental spatial effects.

The results for neutron imaging with experimental spatial effects are shown to contrast with the previous results.



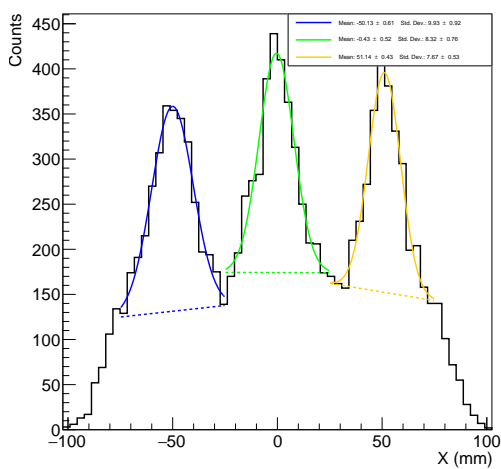


Figure 6.2.5: Neutron imaging projection in the X direction with experimental spatial effects for neutron radiation

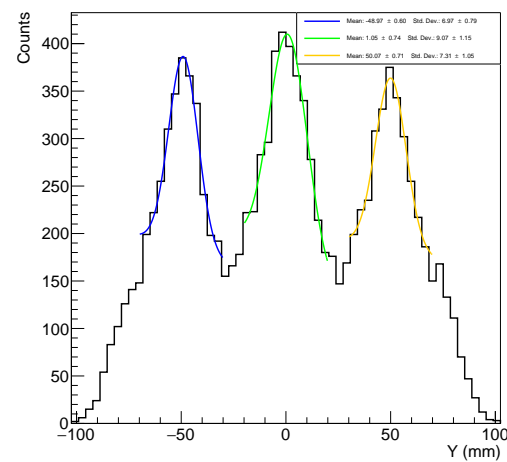


Figure 6.2.6: Neutron imaging projection in the Y direction with experimental spatial effects for neutron radiation

CHAPTER 7

Conclusions

Appendix

APPENDIX A

Point Type	X centroid	Y centroid	X ideal position	Y ideal position	FWHM
▼	14.11000	-13.930000	21.3600	-19.680	7.18275
▼	12.89000	-12.470000	16.3600	-14.680	7.06500
▼	9.29000	-8.710000	11.3600	-9.680	5.88750
▼	6.54000	-5.500000	4.9200	-5.150	4.71000
▼	-0.08000	-0.150000	-0.0800	-0.150	5.41650
▼	-4.81000	4.700000	-5.0800	4.850	5.41650
▼	-8.67000	8.910000	-10.0800	9.850	5.41650
▼	-9.12000	11.920000	-15.0800	14.850	4.71000
▼	-10.20000	11.410000	-20.0800	19.850	4.52160
▲	0.77000	5.330000	-0.0800	4.850	3.17925
▲	-0.33000	10.150000	-0.0800	9.850	4.71000
▲	-0.89000	11.810000	-0.0800	14.850	4.35675
▲	-0.21350	-4.870160	0.0471	-5.295	5.18100
▲	-0.40160	-9.911450	0.0471	-10.295	5.29875
▲	-0.42656	-14.108400	0.0471	-15.295	5.18100
◆	-14.07500	-16.725200	-19.9529	-20.295	5.93460
◆	-12.51700	-13.738000	-14.9529	-15.295	5.65200
◆	-9.38100	-9.443800	-9.9529	-10.295	5.01615
◆	-5.10510	-5.033900	-4.9529	-5.295	5.41650
◆	0.04710	-0.295000	0.0471	-0.295	5.18100
◆	5.24757	5.259160	5.0471	4.705	5.51070
◆	10.45200	9.856660	10.0471	9.705	4.92195
◆	14.17250	12.968600	15.0471	14.705	5.06325
◆	16.40770	12.719800	20.0471	19.705	4.71000
■	5.34590	0.395500	5.0471	-0.295	4.82775
■	10.54430	0.277470	10.0471	-0.295	5.08680
■	14.93090	0.277610	15.0471	-0.295	5.18100
■	-5.29842	0.055734	-4.9529	-0.295	4.94550
■	-9.86571	0.142842	-9.9529	-0.295	4.71000

Table A.0.1: X centroid, Y centroid, X ideal position, Y ideal position, and FWHM of the measured positions.

APPENDIX B

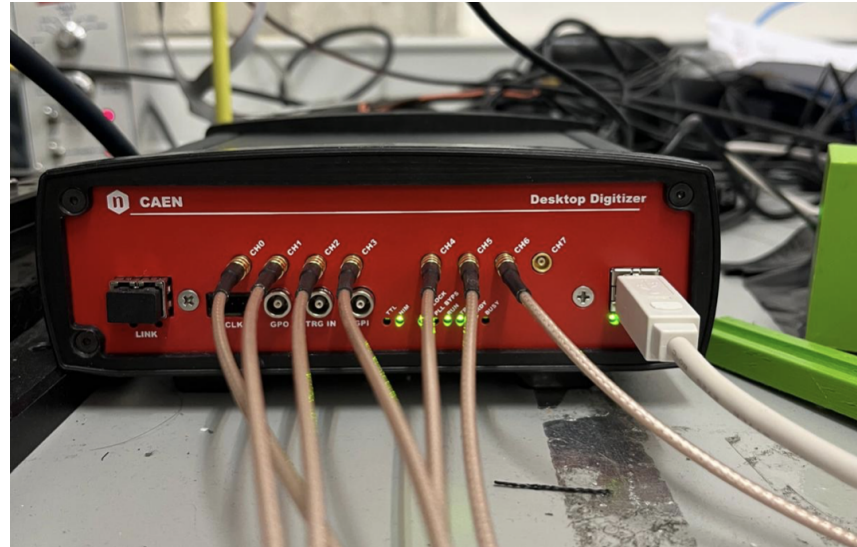


Figure B.0.1: Caption

Ch	Detector	Signal	Goal / Settings DACQ
0	CLYC6 + SiPM	Sum	Energy
1	CLYC6 + SiPM	X- (1 AIT)	Position
2	CLYC6 + SiPM	X+ (2 AIT)	Position
3	CLYC6 + SiPM	Y- (3 AIT)	Position
4	CLYC6 + SiPM	Y+ (4 AIT)	Position
5	CLYC6 + PMT	only signal	Energy / PSD
6	CLYC6 + SiPM	Sum	PSD

Table B.0.1: Your table caption here

Parameter	Board	CH0	CH1	CH2	CH3	CH4	CH5	CH6	CH7
Enable									
Record length	6992 ns	<input type="checkbox"/>							
Pre-trigger	96 ns								
Polarity	Negative								
N samples baseline	256 samples								
Fixed baseline value	0	0	0	0	0	0	0	0	0
DC Offset	20.000 %	20.000 %	20.000 %	20.000 %	20.000 %	20.000 %	20.000 %	20.000 %	20.000 %
Input dynamic	2.0 Vpp								
Discriminator									
Parameter	Board	CH0	CH1	CH2	CH3	CH4	CH5	CH6	CH7
Discriminator mode	Leading edge								
Threshold	45 lsb	170 lsb	55 lsb	55 lsb	45 lsb	45 lsb	40 lsb	185 lsb	45 lsb
Trigger holdoff	1024 ns								
CFD delay	6 ns								
CFD fraction	75%	75%	75%	75%	75%	75%	75%	75%	75%
Input Smoothing	Disabled								
QDC									
Parameter	Board	CH0	CH1	CH2	CH3	CH4	CH5	CH6	CH7
Energy coarse gain	40 fC/(LSB x Vpp)	640 fC/(LSB x Vpp)	40 fC/(LSB x Vpp)	40 fC/(LSB x Vpp)	40 fC/(LSB x Vpp)	40 fC/(LSB x Vpp)	40 fC/(LSB x Vpp)	40 fC/(LSB x Vpp)	40 fC/(LSB x Vpp)
Gate	5000 ns	6500 ns	5000 ns	5000 ns	5000 ns	5000 ns	1400 ns	600 ns	5000 ns
Short gate	100 ns	80 ns	100 ns	100 ns					
Pre-gate	50 ns	0 ns	50 ns	50 ns	50 ns	50 ns	24 ns	50 ns	50 ns
Charge pedestal en.	<input type="checkbox"/>								
Charge pedestal	1024 lsb								
Spectra									
Parameter	Board	CH0	CH1	CH2	CH3	CH4	CH5	CH6	CH7
Energy N channels	16384	16384	16384	16384	16384	16384	16384	16384	16384
PSD N channels	4096								
Time intervals N channels	8192								
Time intervals Tmin	0.000 us								
Time intervals Tmax	1000000 us								
Start/stop Δt N channels	8192								
Start/stop Δt Tmin	-1000 ns								
Start/stop Δt Tmax	1000 ns								
2D Energy N channels	1024								
2D PSD N channels	1024								
2D Δt N channels	128								
Rejections									
Parameter	Board	CH0	CH1	CH2	CH3	CH4	CH5	CH6	CH7
Saturation rejection	<input type="checkbox"/>								
Pileup rejection	<input type="checkbox"/>								
PUR gap	1000 lsb								
E low cut	0.000	0.000	0.000	0.000	0.000	0.000	0.000	0.000	0.000
E high cut	0.000	0.000	0.000	0.000	0.000	0.000	0.000	0.000	0.000
E cut enable	<input type="checkbox"/>								
PSD low cut	0.000	0.000	0.000	0.000	0.000	0.000	0.000	0.000	0.000
PSD high cut	0.000	0.000	0.000	0.000	0.000	0.000	0.000	0.000	0.000
PSD cut enable	<input type="checkbox"/>								
Time intervals low cut	0 ns								
Time intervals high cut	0 ns								
Energy calibration									
Parameter	Board	CH0	CH1	CH2	CH3	CH4	CH5	CH6	CH7
Coincidence Mode	Disabled								
Coincidence window	96 ns								

Figure B.0.2: CAEN DAC configuration for the experimental setup used for neutron irradiation.

Bibliography and References
